Biophysical Journal
Article

Biophysical Society

Antimargination of Microparticles and Platelets in the Vicinity of Branching Vessels

Christian Bächer,[1,*] Alexander Kihm,[2] Lukas Schrack,[1,3] Lars Kaestner,[4] Matthias W. Laschke,[5] Christian Wagner,[2,6] and Stephan Gekle[1]

[1]Biofluid Simulation and Modeling, Theoretische Physik, Universität Bayreuth, Bayreuth, Germany; [2]Experimental Physics, Saarland University, Saarbrücken, Germany; [3]Institute for Theoretical Physics, University of Innsbruck, Innsbruck, Austria; [4]Institute for Molecular Cell Biology, Research Centre for Molecular Imaging and Screening, Center for Molecular Signaling, Medical Faculty, Saarland University, Homburg/Saar, Germany and [5]Institute for Clinical & Experimental Surgery, Saarland University, Homburg/Saar, Germany; and [6]Physics and Materials Science Research Unit, University of Luxembourg, Luxembourg City, Luxembourg

ABSTRACT We investigate the margination of microparticles/platelets in blood flow through complex geometries typical for in vivo vessel networks: a vessel confluence and a bifurcation. Using three-dimensional lattice Boltzmann simulations, we confirm that behind the confluence of two vessels, a cell-free layer devoid of red blood cells develops in the channel center. Despite its small size of roughly 1 μm, this central cell-free layer persists for up to 100 μm after the confluence. Most importantly, we show from simulations that this layer also contains a significant amount of microparticles/platelets and validate this result by in vivo microscopy in mouse venules. At bifurcations, however, a similar effect does not appear, and margination is largely unaffected by the geometry. This antimargination toward the vessel center after a confluence may explain earlier in vivo observations, which found that platelet concentrations near the vessel wall are seen to be much higher on the arteriolar side (containing bifurcations) than on the venular side (containing confluences) of the vascular system.

INTRODUCTION

Red blood cells fill up to 45 percent of the volume of human blood (1–5) and thus represent by far the major cellular blood constituent. Because of their high deformability, red blood cells flowing through a cylindrical channel or blood vessel prefer the low-shear-rate region in the center of the channel. By hydrodynamic interactions with the red blood cells, stiffer particles such as platelets, white blood cells, or artificial drug-delivery agents are thus expelled toward the wall. This separation of red blood cells and stiffer particles is known as margination and is essential for the ability of blood platelets to quickly stop bleeding or for drug delivery agents to closely approach the endothelial wall. One of the first observations of margination studied white blood cells in vivo as well as an in vitro model system containing disks and spheres already in 1980 (6). Interestingly, an in vivo study by Woldhuis et al. (7) demonstrated a striking difference between the platelet distribution in arterioles and venules, with significantly more margination occurring on the arteriolar side of the vascular system. Since then, more detailed insights were gained by experimental studies (8–19), computer simulations (20–41), and theoretical modeling (42–46). These studies all deal with margination in spatially constant geometries such as shear flow, pipes with cylindrical or rectangular cross sections, and plane Couette systems.

In contrast, in living organisms, blood vessels form a hierarchical structure in which large arteries branch all the way down to microcapillaries in a series of bifurcations followed by a reversed series of confluences leading up to larger and larger vessels on the venular side. The typical distance between two bifurcations lies within 0.4 mm up to 1 mm in the microvascular system (2,4). Despite their importance, studies on red blood cell distribution and margination using spatially varying geometries are surprisingly scarce. Platelets have been studied by two-dimensional (2D) simulations in the vicinity of an aneurysm (47,48) and in the recirculation zone behind a sudden expansion of a channel (49). Near a vessel constriction, the locally varying distribution of red blood cells (50–52) and rigid microparticles in suspension with red blood cells have been investigated (53–56). In (56), a local increase in microparticle concentration in front of the constriction has been reported. On a technical side, microchannels including

Submitted November 20, 2017, and accepted for publication June 5, 2018.

*Correspondence: christian.baecher@uni-bayreuth.de

Editor: Jochen Guck.

https://doi.org/10.1016/j.bpj.2018.06.013

bifurcations are investigated as a possible basis for microdevices separating blood plasma (57,58). In asymmetric branches, the Zweifach-Fung effect (59,60) describes an asymmetric red blood cell distribution, i.e., a larger hematocrit in the large flow rate branch (61,62). Under certain circumstances, even an inversion of the Zweifach-Fung effect may occur (63). Combining experiments and simulations in a rectangular channel with bifurcation (64) and for a diverging and converging bifurcation using 2D simulations (65), a cell-depleted zone right after the confluence has been reported. Downstream a bifurcation asymmetry of red blood cell distribution has been seen (57,64,66,67). Reference (68) reported margination of hardened red blood cells while flowing through branching vessels. Balogh and Bagchi (69) investigated the transient behavior of red blood cell motion in more complex networks (69–71). Besides the red blood cell behavior, it is important to consider suspended particles like blood platelets or synthetic particles because possible influences of bifurcations and confluences may play a major role in medical applications. Nevertheless, systematic studies covering particle blood suspensions in networks are scarce. White blood cell motion in asymmetric bifurcations has been studied experimentally in the context of a branched vessel geometry (72), whereas Sun et al. (73) investigated the interaction of six red blood cells flowing behind a white blood cell in the vicinity of vessel junctions.

In this report, we study the margination of stiff spherical particles suspended among red blood cells in the vicinity of vessel confluences and bifurcations. This allows us first to confirm and investigate quantitatively the previously observed cell-depleted layer of red blood cells after confluences. Second, we provide results on the influence of network geometries on stiff particle margination. Our generic stiff particles are a model for artificial drug delivery agents but also serve as a reasonable approximation for blood platelets. We investigate two cylindrical branches either bifurcating from or forming a confluence into a larger vessel by means of three-dimensional (3D) lattice Boltzmann simulations. To realize simulations of these systems, we implement inflow and outflow boundary conditions to the lattice Boltzmann/immersed boundary algorithm similar to an approach based on dissipative particle dynamics by Lykov et al. (74). Behind a vessel confluence, we observe a red blood cell-free layer in the center of the channel persisting for up to 100 μm after the confluence. Importantly, this central cell-free layer is not only devoid of red blood cells but also contains a significant amount of antimarginated microparticles/platelets. Using fluorescent microparticles in mouse microvessels, we consistently observe this antimargination also in vivo. At bifurcations, no equivalent effect occurs. Our findings may explain in vivo observations of Woldhuis et al. (7), who found that in the vascular system, platelet margination is strongly present at the arteriolar side with bifurcations but less at the venular side with confluences. Similarly, recent observations show that thrombi formed in arterioles contain significantly more platelets than thrombi formed in venules (75), which is another indication of increased platelet margination on the arteriolar side. By considering the axial distribution of microparticles along the flow direction, we furthermore reveal the site of confluence as a spot with locally increased concentration. The article is organized as follows: we first introduce the simulation and experimental methods and then report 2D and one-dimensional (1D) concentration profiles first in the system with vessel confluence, including the experimental results, then in the system with a bifurcation. Finally, we investigate the influence of larger hematocrit and microparticle distribution in an asymmetric bifurcation.

METHODS

Lattice Boltzmann/immersed boundary method

Fluid flow in the confluence/bifurcation geometry is modeled using the 3D lattice Boltzmann method (LBM), which calculates fluid behavior by a mesoscopic description (76–78). We use the implementation of LBM in the framework of the simulation package ESPResSo (79–81). Red blood cells and particles are modeled using the immersed boundary method (IBM) (37,56,82,83).

To mimic realistic conditions of blood flow, we assign the blood plasma density $\rho_{plasma} = 1000\,\mathrm{kg/m^3}$ and viscosity $\mu_{plasma} = 1.2 \times 10^{-3}$ Pas. Due to the large size of the red blood cells and microparticles, we expect the temperature to hardly affect collective flow behavior of cells and particles and thus neglect the effect of thermal fluctuations. A typical fluid grid of these simulations contains $170 \times 110 \times 58$ nodes for a bifurcation and $288 \times 110 \times 58$ nodes for a confluence. The time step is chosen as 0.09 μs, with the time of a typical simulation being about 2.5 s.

Red blood cells and microparticles are realized by an infinitely thin elastic membrane interacting with the fluid. For the calculation of elastic forces imposed on the fluid, the membrane is discretized by nodes that are connected by triangles. A red blood cell possesses 1280 triangles and 642 nodes and has a diameter of 7.82 μm. The averaged distance between neighboring nodes is about one LBM grid cell. Nodes transfer forces to the fluid and are themselves convected with the local fluid velocity. Interpolation between membrane nodes and fluid nodes is done using an eight-point stencil. The viscosity contrast of the cells is $\lambda = \eta_{in}/\eta_{out} = 1$, i.e., the fluid inside and outside the cells has the same viscosity. The elastic properties of a red blood cell are achieved by applying the Skalak model (5,84,85) with a shear modulus $k_S = 5 \times 10^{-6}$ N/m and an area dilatation modulus $k_A = 100 k_S$. Additional bending forces are computed on the basis of the Helfrich model using a bending modulus $k_B = 2 \times 10^{-19}$ Nm (5,86,87). For the calculation, the algorithm denoted method A in (86) is used with the bending energy being proportional to the angle of adjacent triangles and the actual forces being computed by analytically differentiating the energy with respect to node position. This somewhat simplistic approach is appropriate for this work, in which we focus on collective rather than detailed single-cell behavior and in which especially the behavior of the microparticles is of interest.

Microparticles are modeled in a similar fashion as the red blood cells with 320 triangles and 162 nodes. The microparticles are chosen to have half the size of red blood cells ($a = 3.2\,\mu$m), which has been reported to show strong margination (32). In contrast to the red blood cells, the microparticles contain an additional inner grid to ensure the stiffness and (approximate) nondeformability of the microparticles (37). The inner grid is linked to the membrane nodes by a harmonic potential. Elastic properties of microparticles are chosen 1000 times larger than for red blood cells. For the purpose of numerical stability, we apply an empirical volume conservation potential (38) as well as a short-ranged soft-sphere repulsion, which decays

with the inverse fourth power of the distance and with a cutoff radius equal to one grid cell. The latter potential acts between all particles and between the particles and the channel wall.

The stability and accuracy of our simulation method have been extensively validated in (37,86). In addition, as detailed in Supporting Materials and Methods, the shapes of isolated red blood cells in cylindrical and rectangular channels have been validated to agree with methodically very different dissipative particle dynamics (88) and boundary integral (89) simulations. The behavior of stiff particles is validated by considering the drag force on a sphere as well as the tumbling of a spheroid in shear flow (90). We also demonstrate that the numerically motivated short-range repulsive force does not affect our results. Finally, we validate our simulation method by comparing the asymmetric red blood cell distribution in bifurcations with recent computational results by Balogh and Bagchi (70) as well as experimental data (61,91).

Channel geometry

The systems of interest, a confluence and a bifurcation, are shown in Fig. 1 *a*. Both geometries are constructed in the same way: a main cylindrical channel of radius R_{ch} branches into two symmetric daughter channels of radius R_{br}. To obtain a smooth boundary, i.e., the boundary itself and the first derivative is continuous, the transition between main channel and the branches is modeled by third-order polynomials: one polynomial, $y_c(x)$, describes the bifurcating centerline, whereas another, $y_{up}(x)$, describes the upper/lower boundary. By rotation around the centerline with radius $y_{up}(x) - y_c(x)$, we obtain a circular cross section for each x forming the bifurcation along the flow direction. Where the cross sections of the two branches overlap, the boundary is left out.

Inflow/outflow boundary condition for IBM-LBM

To investigate a confluence and a bifurcation as displayed in Fig. 1 *a*, periodic boundary conditions cannot be employed. Joining both geometries into one very large system would be computationally far too expensive because of the very long-range influence of bifurcations/confluences, as will be detailed in the course of this work. At the same time, at the entrance of the branches in Fig. 1 *a* (*left*) as well as at the entrance of the main channel in Fig. 1 *a* (*right*), we do not want the microparticles and red blood cells to enter in a randomly distributed fashion but instead obey a marginated configuration to match with the well-known behavior in a long tube. The purpose behind this inflow condition is to bring out clearly how the behavior of the marginated fraction of microparticles is influenced by the confluence/bifurcation.

To meet these requirements, we implemented inflow and outflow boundary conditions to our IBM-LBM algorithm similar to a recent work using dissipative particle dynamics (74). We start by simulating straight cylinders with periodic boundaries and a body force driving the flow, as depicted at the top of Fig. 1 *b*. These feeding simulations yield a time-dependent sequence, which then serves for particle inflow in the complex system of interest. During the simulation of the complex system, we check a frame of the feeding sequence for cells and particles crossing a certain (arbitrary) plane. Particles crossing this plane are then inserted at the same radial position with the same shape into the complex system, as illustrated also in Fig. 1 *b*. For crossing of the plane, the center-of-mass serves as a criterion similar to (74). The inflow velocity is chosen to match the flow rate prescribed in the straight cylinder. To prevent overlap of cells during inflow, we sometimes increase the flow rate slightly (~10%). As a result, we obtain a marginated pattern at the entrance of our complex systems, as proven by the cross-sectional concentration profiles shown in Supporting Materials and Methods.

Because azimuthal motion of the dilute microparticles in the feeding channels is extremely slow, even a very long feeding simulation would lead to a biased distribution of microparticles upon entering the complex channel. This is prevented by applying a small angular random force to the microparticles in the feeding channel, thus guaranteeing an azimuthally homogenous, yet well marginated distribution of microparticles. We furthermore show in Supporting Materials and Methods that after a first filling of the system, the cell and particle number in the system reaches a plateau and slightly fluctuates around a constant value.

For the fluid, to prescribe a distinct flow rate, we assign a constant velocity to all fluid LBM nodes at the beginning of the simulation box. The same is done at the end of the box, taking into account the different cross sections of the main channel and branches, thus matching fluid inflow and outflow. About 15 grid cells behind the inflow, the flow profile matches tube flow. This region with evolving flow profile is skipped for particle inflow and in data analysis.

Analysis

In our work, we employ different concentration profiles at given positions along the channel. First, we compute cross-sectionally averaged concentrations, leading to 1D concentration profiles as a function of position along the flow direction x. Some of these profiles consider only a certain fraction of cells or particles entering the channel in specific regions, which are labeled as a function of their lateral (r,ϕ) position in polar coordinates at the entrance of the system. Corresponding concentrations are calculated, taking into account only this particular fraction of cells or particles. The

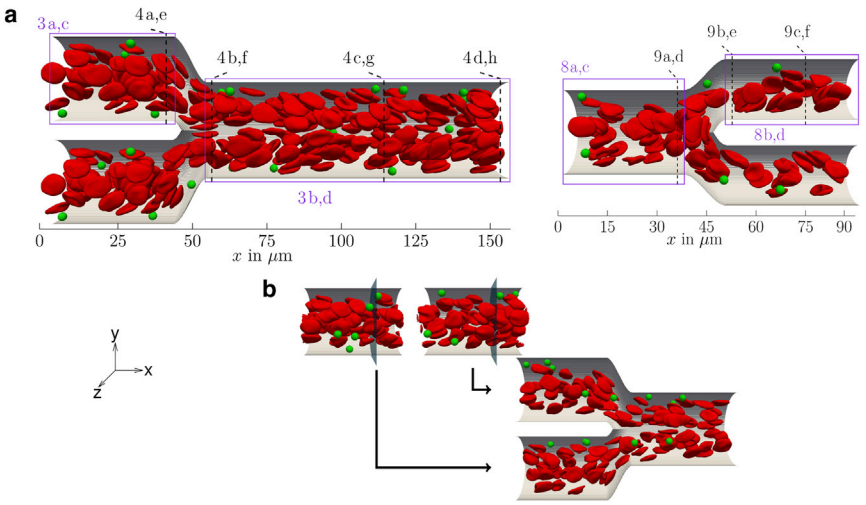

FIGURE 1 (*a*) Systems of interest: a suspension of red blood cells and microparticles flowing either through a confluence (*left*) or a bifurcation (*right*). Rectangles with numbers refer to figures containing corresponding 2D radial/planar projections, whereas dashed lines refer to figures containing cross-sectional profiles. (*b*) Inflow is realized using straight cylinders as feeding systems: whenever a cell/particle crosses the indicated plane, it is fed into one of the branches of the confluence system. To see this figure in color, go online.

labeling is illustrated by the color code in Fig. 2 *a* and by the criteria for r and ϕ in Fig. 2 *b*.

Second, we use three types of 2D concentration profiles. For microparticle concentrations, 2D radial projections in the r,x plane are calculated, which reflect the radial symmetry of the main and the branch channels. Such projections, however, are not appropriate to understand nonradially symmetric effects occurring near confluences or bifurcations. We thus employ in addition, mainly for red blood cell concentrations, planar projections of the 3D concentrations on the y,x plane by integrating the concentration over the z direction perpendicular to the plane of the paper. Finally, to get further insight into cell and particle distributions perpendicular to the flow direction, we calculate cross-sectional profiles within the y,z plane.

All concentration profiles are averaged over the whole simulation time, starting from the moment at which the number of cells and particles does not vary significantly.

Preparation of dorsal skinfold chamber and in vivo imaging

Animals

The in vivo experiments were performed in 10–12 week old male C57BL/6 mice (n = 3) with a body weight of 23–26 g. The animals were bred and housed in open cages in the conventional animal husbandry of the Institute for Clinical & Experimental Surgery (Saarland University, Saarbrücken, Germany) in a temperature-controlled environment under a 12 h/12 h light-dark cycle and had free access to drinking water and standard pellet food (Altromin, Lage, Germany). The experiment was approved by the local governmental animal care committee (approval number 06/2015) and was conducted in accordance with the German legislation on protection of animals and the National Institutes of Health Guidelines for the Care and Use of Laboratory Animals (Institute of Laboratory Animal Resources, National Research Council, Washington).

Dorsal skinfold chamber model

Microvessels were analyzed in the dorsal skinfold chamber model, which provides continuous microscopic access to the microcirculation of the striated skin muscle and the underlying subcutaneous tissue (92). For the implantation of the chamber, the mice were anesthetized by i.p. injection of ketamine (75 mg/kg body weight; Ursotamin; Serumwerke Bernburg, Bernburg, Germany) and xylazine (15 mg/kg body weight, Rompun; Bayer, Leverkusen, Germany). Subsequently, two symmetrical titanium frames (Irola Industriekomponenten KG, Schonach, Germany) were implanted on the extended dorsal skinfold of the animals, as described previously in detail (93). Within the area of the observation window, one layer of skin was completely removed in a circular area of ~15 mm in diameter. The remaining layers (striated skin muscle, subcutaneous tissue, and skin) were finally covered with a removable cover glass. To exclude alterations of the microcirculation due to the surgical intervention, the mice were allowed to recover for 48 h.

In vivo microscopy

In vivo microscopic analysis was performed, as previously described (94). In detail, the mice were anesthetized, and a fine polyethylene catheter (PE10, 0.28 mm internal diameter) was inserted into the carotid artery for application of the plasma marker 5% fluorescein-isothiocyanate-labeled dextran 150,000 (Sigma-Aldrich, Taufkirchen, Germany) and microspheres (Fluoresbrite Plain YG 1.0 μm; Polysciences, Warrington, PA). Then, the animals were put in lateral decubital position on a plexiglass stage, and the dorsal skinfold chamber was attached to the microscopic stage of an upright microscope (Axiotech; Zeiss, Jena, Germany) equipped with an LD EC Epiplan-Neofluar 50×/0.55 long-distance objective (Zeiss) and a 100 W mercury lamp attached to a filterset (excitation 450–490 nm, emission > 520 nm). The microscopic images were recorded using a complementary metal-oxide semiconductor video camera (Prime 95B; Photometrics, Tucson, AZ) at an acquisition speed of 415 images per second controlled by a personal-computer-based acquisition software (NIS-Elements; Nikon, Tokyo, Japan).

Trajectory analysis

The recorded video sequence was analyzed using a single-particle tracking algorithm. Hereby, the intensity profile of each frame was adjusted to have both the top and bottom 1% of all pixels saturated, correcting for changes in illumination and exposure time. With the aid of a tailored MATLAB (The MathWorks, Natick, MA) script, all spherical (round) objects were detected and interconnected among all frames by cross correlating consecutive images. To only detect microspheres (and not red blood cells), we set a threshold of 0.9 as a lower limit in normalized intensity values because they are fluorescent. Further, we defined a minimal diameter for the detected particles (0.7 μm), causing a trajectory to end if the measured value falls below this value. Combining the coordinates of all classified microspheres in this way over the whole video sequence, we derived the respective trajectories.

RESULTS AND DISCUSSION

Channel confluence

We first investigate the system with two branches of radius 16 μm merging into one main channel of radius 17.5 μm, as depicted in Fig. 1 *a* (*left*) and shown in Video S1. Results for a larger/smaller main channel are qualitatively similar and shown in the Supporting Materials and Methods. The centerlines of the two branches are separated by 39 μm, and the transition zone from the end of the branches to the beginning of the main channel is about 13 μm. We choose the mean velocity at the entrance of our system to be about $v = 2.5$ mm/s. Simulations are first performed for a physiologically realistic hematocrit (red blood cell volume fraction) of $Ht = 12\%$. Results for a higher $Ht = 20\%$ are qualitatively similar and are presented at the end of this contribution. The Reynolds

a

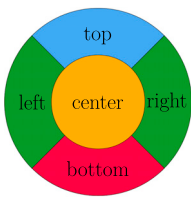

b

	r	ϕ
center	$r <= R_{ch}/2$	$\forall\phi$
top	$r > R_{ch}/2$	$45 <= \phi < 135$
bottom	$r > R_{ch}/2$	$225 <= \phi < 315$
left	$r > R_{ch}/2$	$135 <= \phi < 225$
right	$r > R_{ch}/2$	$315 <= \phi \ \& \ \phi < 45$

FIGURE 2 (*a*) Color labeling and (*b*) labeling criteria for red blood cells and microparticles at the entrance of the system with respect to the in-plane position in the cross section. Because of symmetry, the particles at left and right can be treated equally. To see this figure in color, go online.

number calculated from the centerline velocity, the red blood cell radius R_{RBC}, and the kinematic viscosity of the fluid ν_{plasma} is $Re = \frac{(R_{RBC} \cdot v)}{\nu} = \mathcal{O}(10^{-2})$.

Cell and particle distribution

We start by considering 2D concentration profiles along the flow direction in Fig. 3. In the two small branches and far away from the confluence, we observe a homogeneous distribution of red blood cells around the center and the cell-free layer with vanishing concentration (95–97) near the wall, as can be seen by Fig. 3 *a*. The microparticle concentration in Fig. 3 *c* exhibits the typical margination peak near the wall. The state of full and azimuthally homogeneous margination is confirmed by the cross sections at channel entrance shown in Supporting Materials and Methods. This behavior is the same as in a straight channel.

Approaching the confluence, we observe an asymmetric cell-free layer; near the inner boundary of the branch, the cell-free layer decreases, whereas near the outer boundary, it increases. The asymmetry becomes more pronounced toward the end of the branches ($x \approx 40\ \mu m$) stemming from cells flowing toward the main channel. However, the motion of red blood cells toward the main channel already initiates at $x \approx 30\ \mu m$, i.e., about 10 μm before the end of the branches. This also affects microparticle behavior, as can be seen by the two separate peaks in the radially projected concentration in Fig. 3 *c*. These two peaks stem from the particles near the inner and the outer boundary, respectively; the microparticles near the inner boundary remain close to the wall, whereas the particles near the outer boundary migrate away from the wall because of the flow profile toward the main channel and the increased cell-free layer.

Entering the main channel, we observe a decreased cell-free layer near the upper and lower boundary in Fig. 3 *b* (*right*) at the beginning. An interesting feature of the red blood cell concentration is the additional cell-free layer that develops in the channel center after the confluence. This agrees well with the findings of (64), which showed that a cell-depleted zone behind the apex of a confluence develops. We confirm that finding by considering the concentration and also highlight the long-range stability of the central cell-free layer.

Most remarkably, this central cell-free layer contains, just like its classical near-wall counterpart, a significant amount of microparticles, as can clearly be seen in the radially projected microparticle concentration of Fig. 3 *d*.

Before investigating further this central cell-free layer, we consider cross-sectional concentration profiles in Fig. 4. In Fig. 4 *a*, we observe how the circular pattern of red blood cells is shifted toward the inner boundary at the end of the branches. This corresponds to the asymmetric cell-free layer in Fig. 3 *a*. Entering the main channel, the pattern of red blood cell concentration possesses two flattened and asymmetric spots (Fig. 4 *b*) clearly separated by the central cell-free layer, which shows vanishing concentration. At the left and right of the main channel, an additional large cell-free spot is obtained. This central-cell-free layer stems from the cells flowing out of the upper and lower branch competing for the channel center.

Microparticles in the two branches remain well marginated until the end of the branches, as shown in Fig. 4 *e*. After the confluence, however, Fig. 4 *f* shows how a notable fraction of microparticles is now located very near the channel center. This can be understood by the original location of the microparticles inside the branches; those microparticles that are located near the inner boundary of the branch enter the main channel in the center. This location is favorable because of the additional central cell-free layer observed in Fig. 4 *b*. In Supporting Materials and Methods, we show the antimargination also for platelet-shaped microparticles. Thus, this geometry leads to a redistribution of

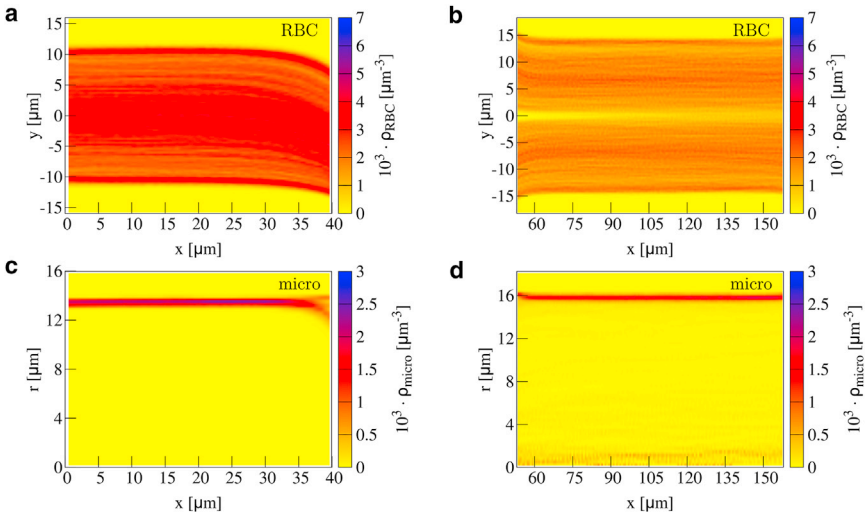

FIGURE 3 Concentration of red blood cells in a confluence in 2D planar projection (*a*) along the upper branch and (*b*) along the main channel. Microparticle concentration in 2D radial projection is shown (*c*) along the upper branch and (*d*) along the main channel. The cell-free layer near the inner boundary decreases at the end of the branches, whereas it increases near the outer boundary. Inside the main channel, an additional cell-free layer in the center develops. To see this figure in color, go online.

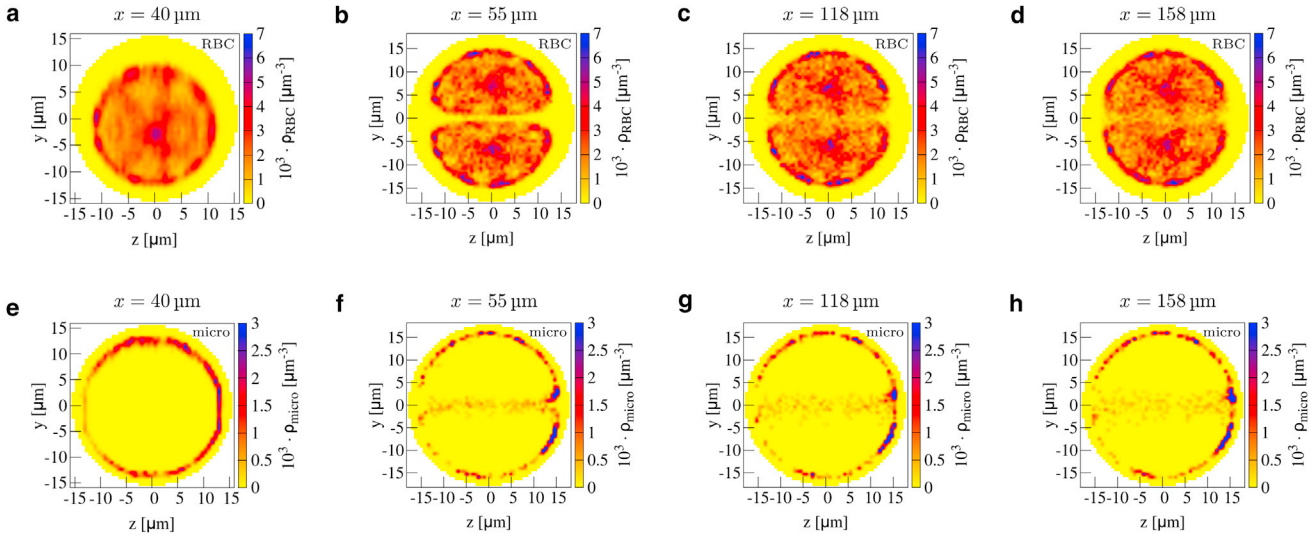

FIGURE 4 2D cross-sectional concentration in a confluence for red blood cells (*a–d*) and microparticles (*e–h*) at the end of the branches (*a* and *e*), at the beginning of the main channel (*b* and *f*), at the middle of the main channel (*c* and *g*), and at the end of the main channel (*d* and *h*). Positions are also indicated by the dashed black lines in Fig. 1 *a*. In the main channel, a clear cell-free layer in the center together with microparticle antimargination is present. To see this figure in color, go online.

microparticles from a near-wall marginated position before the confluence to a near-center antimarginated position after the confluence.

Lifetime of the central cell-free layer, antimargination, and physiological consequences

An interesting question is the stability of the red blood cell-depleted central cell-free layer and the corresponding antimarginated microparticles as the flow continues away from the confluence location along the main channel. Fig. 3 *b* shows that the central cell-free layer is surprisingly stable, being visible all along the main channel and only becoming slightly blurred toward the end. The same trend can be observed in the cross-sectional concentration at three sites along the main channel in Fig. 4, *b–d*. Although it starts to become blurred after 60 μm in Fig. 4 *c*, the central cell-free layer and especially the cell-free spot left and right is visibly present until at least 100 μm behind the confluence, as shown in Fig. 4 *d*. Similarly, the corresponding microparticle concentration in Fig. 4, *f–h* shows that microparticles are located in the center all along the main channel. Thus, a confluence of two channels influences microparticle behavior over distances that are much longer than the channel diameter.

To gain a more mechanistic insight into this long-time stability of the central cell-free layer, we calculate the (shear-induced) diffusion coefficient (23,25,97–101) of red blood cells in the center. For this, we compute the time-dependent mean-square displacement, which is shown in Supporting Materials and Methods. By modeling the increase in mean-square displacement with time by the theoretical expectation for normal diffusion $\langle \Delta y(t)^2 \rangle = 2Dt$, we extract a diffusion coefficient for the red blood cells of $D_{RBC} \approx 28\ \mu m^2/s$ in the case of $Ht = 12\%$. This value is of the same order as that of previous results in experiments with red blood cells (98,99,101) and simulations of spheres and platelets (23,25). By assuming a thickness of 1.5 μm and a flow speed of 2.5 mm/s, we calculate a distance of 100 μm required to bridge the central cell-free layer. This length scale agrees well with the observation in the concentration profiles that the central cell-free layer starts to become blurred after 100 μm. We calculate in the same way the shear-induced diffusion coefficient of the microparticles $D_{micro} \approx 25\ \mu m^2/s$. Reference (98) reports for platelets in a perfusion chamber 34 $\mu m^2/s$ for a shear rate of 8321/s and unknown hematocrit. References (23,25) obtain a diffusivity of a factor 2 smaller in simulations of plane Couette flow with $Ht = 0.2$. Considering not only the gap of the central cell-free layer to be closed but also the larger spot left/right (assuming a distance of 5 μm to be bridged), we can estimate a distance of 1.1 mm for red blood cell redistribution, which is comparable to the estimation of 25 times the channel diameter by Katanov et al. (97). When we estimate the length scale required for microparticles to migrate toward the channel wall, i.e., to marginate, we get ~5 mm. Comparing this to the typical distance between successive confluences of ~0.4–1 mm (2,4), we conclude that full margination cannot be regained. This in turn may explain the in vivo observations that on the venular side of the vascular system, margination is much less pronounced than on the arterioral side (7,75).

Furthermore, we want to address the question of how strong the effect of antimargination is. Therefore, we calculate the fraction of particles that are not located directly next to the wall, i.e., we consider particles that are more than one particle radius away from the vessel wall. For the

concentration profiles in Fig. 4, we obtain the fractions 0 at $x = 40$ μm, 0.158 at $x = 55$ μm, 0.138 at $x = 118$ μm, and 0.135 at $x = 158$ μm. We find that the fraction decreases very slowly with increasing distance from the confluence because of marginating microparticles (most likely those located *left*/*right*).

Axial concentration

Further insight can be gained by considering 1D axial cell and particle concentration profiles in Fig. 5. The overall red blood cell concentration exhibits two plateaus inside the main channel and inside the branches, respectively. Inside the branches, the concentration is lower than in the main channel, which is in agreement with the Fahraeus effect (102). Right at the confluence, we observe a zone in which the red blood cells become slightly depleted. The microparticle concentration along the branches first increases slightly, and right at the confluence, a strong peak develops. In the main channel, the microparticles have a nearly constant concentration.

To elucidate red blood cell behavior further and especially to explain the peak in microparticle concentration, we label the cells/particles while entering the branches, as explained in Methods. The concentrations for the labeled cells and particles are shown in Fig. 6.

The red blood cells in the center, those left/right, and those at the bottom of the branches behave in a similar fashion: at the end of the branches, they are accelerated and thus have a decreased concentration. After a small peak, they quickly reach a constant concentration in the main channel. Only the cells arriving at the top exhibit a slightly increasing concentration at the end of the branches but are depleted as well at the site of the confluence. Microparticles arriving left/right or at the bottom show a similar concentration profile as that of the corresponding red blood cells and thus do not cause the peak in overall concentration in Fig. 5. We note that these concentration profiles can be understood by passive tracer particles similar to those in constricted channels (56) and as detailed in Supporting Materials and Methods. From Fig. 6 *b*, we are thus able to conclude that the peak stems from the microparticles flowing at the top of the branches. The concentration of these microparticles increases more than twofold compared to the branches and the main channel. Because of the margination, the microparticles are located right beside the wall. Also, the concentration profile of the microparticles at the top can be reproduced by passive tracer particles, as done in Supporting Materials and Methods. Thus, the local increase in microparticle concentration can be understood by the underlying flow profile.

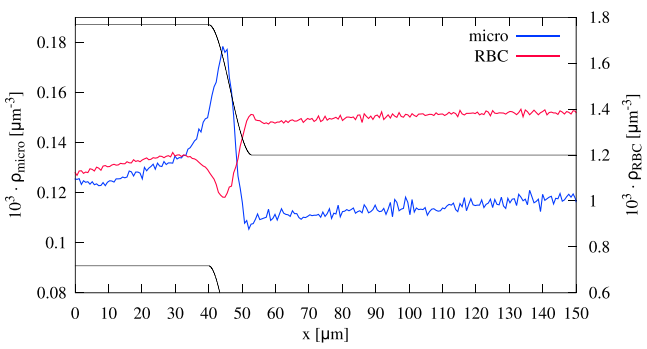

FIGURE 5 1D axial profile of red blood cells and microparticles flowing through a vessel confluence. Whereas the red blood cells are depleted at the site of the confluence, the microparticles exhibit a concentration increase of ~50% compared to the branches and the main channel. To see this figure in color, go online.

In vivo observation of microparticle antimargination

To demonstrate the relevance of the antimargination observed in our simulations, we inject fluorescent beads into living mice and image their behavior when flowing through a microvessel confluence. In Fig. 7, we show a set of trajectories obtained from the video of microscopy images (corresponding Video S2). In agreement with the predictions of our numerical simulations, beads that are initially marginated at the outer walls (*blue lines* in Fig. 7) remain marginated, whereas beads located initially at the inner walls (*red lines* in Fig. 7) undergo antimargination and end up near the channel center after passing through the confluence.

Channel bifurcation

Next, a bifurcation is investigated, as depicted in Fig. 1 *a* (*right*) and shown in Video S3. The suspension of red blood cells and microparticles flows through a straight channel of radius 16 μm, branching into two daughter channels of radius 11.5 μm. The main channel and the combined branches have the same cross-sectional area, and the centerlines of the two branches are separated by 34 μm. The transition zone from the end of the main channel to the beginning of the branches is about 13 μm.

Cell and particle distribution

In Fig. 8, we first investigate the 2D concentration of red blood cells and microparticles along the flow direction. At the very beginning, around $x \approx 0$, we again observe a homogeneous red blood cell distribution (Fig. 8 *a*) around the center and the cell-free layer with vanishing red blood cell concentration near the wall. Approaching the bifurcation, the cell-free layer decreases. The decrease in cell-free layer is of the same amount at both locations near the upper boundary and near the lower boundary. It can be straightforwardly explained by the bifurcating geometry, which causes the red blood cells to flow upwards/downwards into the daughter channels. This motion into the daughter channels starts already ~10 μm before the end of the main channel and makes the cells migrate toward the outer wall.

An asymmetry in the cell-free layer occurs inside the daughter channels (Fig. 8 *b*), as also observed in recent

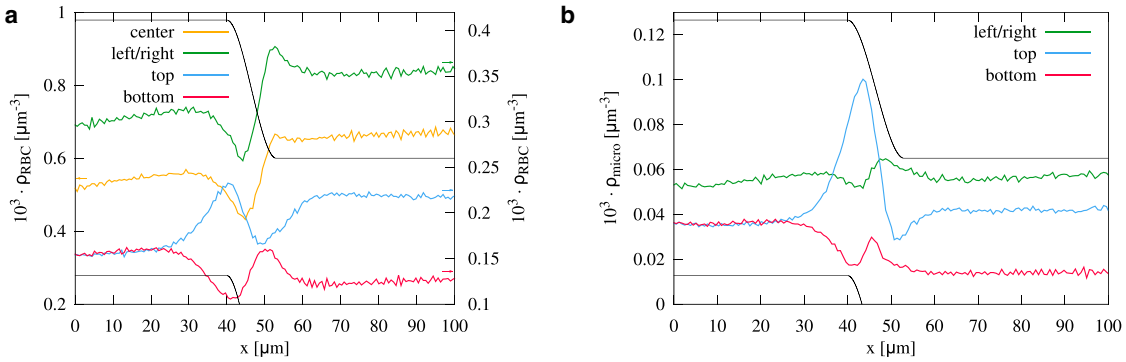

FIGURE 6 Axial concentration of (*a*) red blood cells and (*b*) microparticles distinguished regarding their position inside the cross section of the branches, as illustrated in Fig. 2. The microparticles entering at the top of the upper branch (or equivalently, the bottom of the lower branch) exhibit a pronounced peak. To see this figure in color, go online.

work (57,67). The asymmetry is especially pronounced at the beginning of the branches, stemming from cells flowing in the center of the main channel, which enter either the upper or lower branch near the inner wall. We observe a strongly decreased cell-free layer near the inner boundary right at the beginning of the daughter branches. The thickness of the cell-free layer near the outer boundary increases correspondingly. After ∼10 μm, the inner and outer cell-free layers both reach a constant value, which is similar to the length scale for the re-establishment of the outer cell-free layer after the confluence. Interestingly, the inner and outer cell-free layers do remain asymmetric and retain this asymmetry until the very end of our channel, ∼50 μm behind the bifurcation.

Although the cell-free layer decreases at the end of the main channel, hardly an effect is observed on microparticle behavior. Entering the branches, the microparticle concentration peak only becomes more blurred because of the microparticles located near the upper boundary entering the larger cell-free layer inside the branch.

The asymmetries in cell and particle distribution can be seen in more detail in the 2D cross-sectional profiles in Fig. 9. At the end of the main channel in Fig. 9 *a*, the red blood cell distribution is still circular, with only small deviations corresponding to the decrease in cell-free layer seen in Fig. 8 *a*. At the beginning of the branch, the circular red blood cell concentration is strongly shifted toward the inner boundary in Fig. 9 *b*, and a less pronounced but still clearly visible asymmetry is still present at the end of the branch in Fig. 9 *c*. Furthermore, a local spot with increased red blood cell concentration is observed near the inner boundary.

Whereas the microparticles are hardly affected at the end of the main channel (Fig. 9 *d*), a notable effect is the vanishing concentration of microparticles near the inner boundary of the branches in Fig. 9, *e* and *f*. Over an angle range of ∼90° at the bottom of Fig. 9, *e* and *f*, the microparticle concentration vanishes completely. The vanishing microparticle concentration can be understood by the radial distribution in the main channel because of margination: to reach positions near the lower boundary of the branch, the microparticles would have to be located near the center of the main channel, which is not the case because of margination. Thus, we report a region within the branches that possesses a vanishing microparticle concentration in comparison to a simple straight channel.

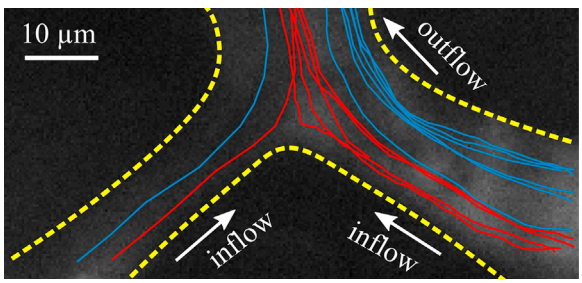

FIGURE 7 In vivo measurement of tracked fluorescent beads in mouse microvessels. Blue lines show trajectories of beads that remain marginated after the bifurcation, whereas red lines show beads undergoing antimargination. Yellow dashed lines denote the vessel boundaries. To see this figure in color, go online.

Axial concentration

As for the confluence, we now investigate the behavior of cells and particles along the varying geometry by 1D axial concentration profiles in Fig. 10. After a constant plateau inside the main channel, both red blood cell and microparticles show a clear peak ahead of the apex of the bifurcation. Inside the branches, the red blood cell take the same concentration as in the main channel, whereas the microparticle concentration decreases. The latter can be explained by the intrinsic velocity profile; flowing beside the boundary, the stiff microparticles cover a certain ring of tube diameter along the boundary. Because of the fixed particle size, this ring has the same diameter in the main channel and within the branches. Assuming a Poiseuille flow and averaging over such a ring around the boundary leads to a higher

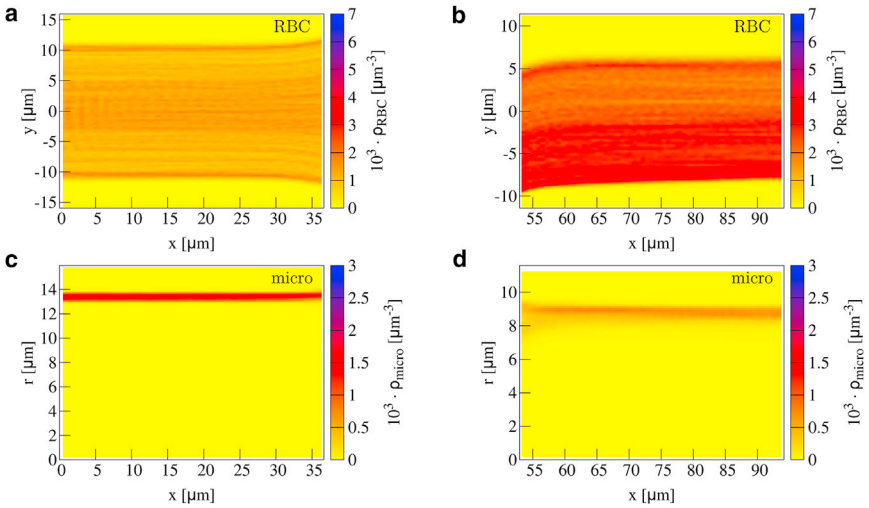

FIGURE 8 2D planar projection within the bifurcation for red blood cells (*a*) along the main channel and (*b*) along the upper branch. 2D radial projection shows microparticle concentration (*c*) along the main channel and (*d*) along the branches. The cell-free layer decreases at the end of the main channel, and we observe an asymmetric cell distribution inside the branches. The margination peak of microparticles is somewhat blurred after the bifurcation but is otherwise unaffected. To see this figure in color, go online.

flow rate inside the branches because they cover a larger part of the steep velocity profile. Thus, within the branch, the microparticles experience a larger velocity, leading to lower residence time, thereby causing a decreasing concentration.

We furthermore distinguish the cells and particles regarding their position inside the main channel and calculate the axial concentration profiles for each cell/particle fraction in Fig. 11, *a* and *b*. All fractions of red blood cells behave in a similar manner with a small peak at the apex. This peak stems from cells being trapped at the apex of the bifurcation; arriving in the center of the main channel, red blood cells have to break symmetry and decide for one branch. As visible in Fig. 1 *a* (*right*), some cells flow directly onto the apex and are trapped there before flowing in one of both branches, a phenomenon called "lingering" in (69). We note that also the red blood cells at the top/bottom show a peak because they are still located close enough to the center to be influenced by more central cells getting trapped at the apex.

In full analogy, a similar peak is observed for microparticles located left/right in Fig. 1 *b*. Also, these microparticles flow onto the apex and become trapped for a short period of time. In contrast, the microparticles located top/bottom are diluted at the bifurcation. After a subsequent little dip in concentration, microparticles from both regions quickly reach a constant concentration inside the branches.

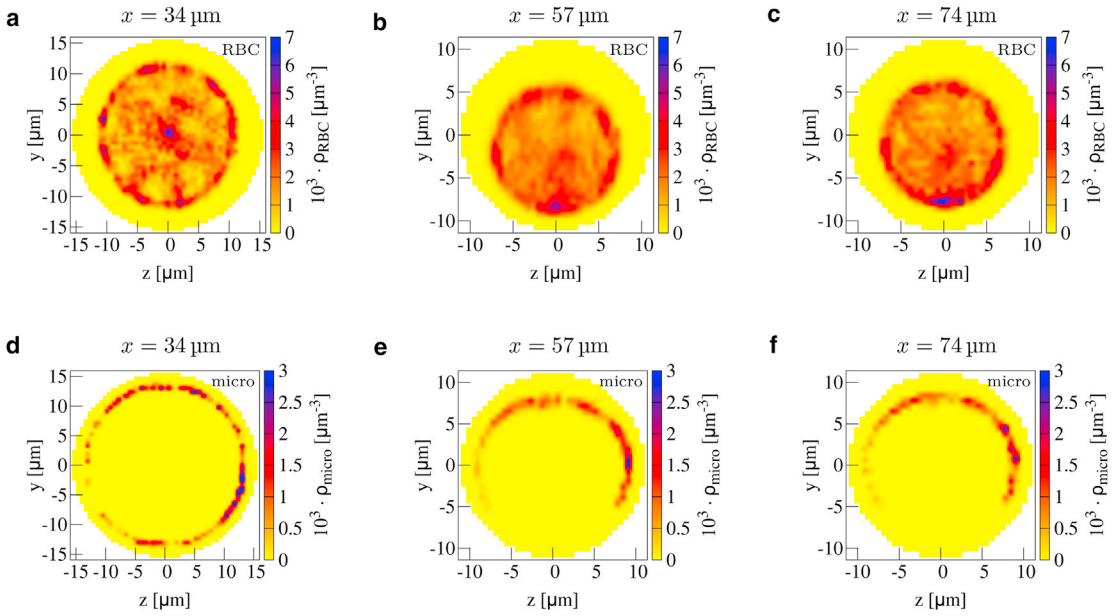

FIGURE 9 2D cross-sectional concentration of red blood cells (*a–c*) and microparticles (*d–f*) at the end of the main channel (*a* and *d*), at the beginning of the branches (*b* and *e*), and at the end of the branches (*c* and *f*). See Fig.1 *a* for indications of the respective positions along the channel. Inside the branches, an asymmetric cell-free layer develops, and microparticles suffer a loss of concentration directly beside the inner wall. To see this figure in color, go online.

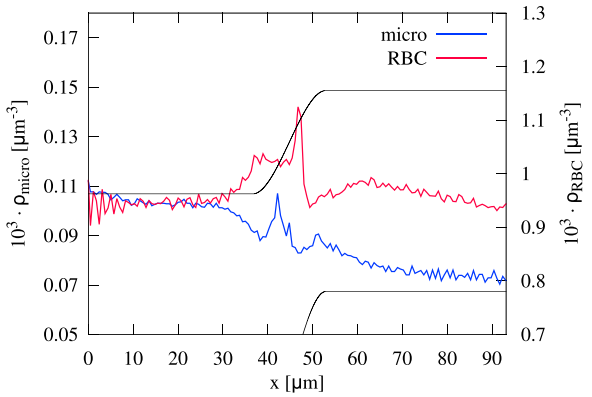

FIGURE 10 Axial concentration of red blood cells and microparticles flowing through a bifurcating channel. Both red blood cells and microparticles exhibit a peak in front of the bifurcation apex. The microparticle concentration increases directly in front of the apex, whereas the red blood cell concentration exhibits a second small peak because of a second cell flowing onto a cell already being stuck at the apex. To see this figure in color, go online.

The concentration profile of both cells and particles can be understood again by considering tracer particles (see Supporting Materials and Methods).

Influence of hematocrit

In the following section, we present simulations that have the same geometrical properties as the channels in Fig. 1 but with a hematocrit of $Ht = 20\%$ for the inflow.

Fig. 12 shows that behind the confluence of two branches, the red blood cell distribution behaves qualitatively similarly to the lower hematocrit. Although the cell-free layer near the vessel wall is reduced compared to Fig. 3 *b*, the cell-free layer in the center of the main channel in Fig. 12 *a* is of about the same size. Only at the left and right of the cross section, the cell-free space clearly reduces compared to the lower hematocrit (Fig. 12 *b*). The central cell-free layer is very pronounced up to 40 μm behind the confluence but becomes blurred slightly faster toward the end of the channel when compared to the low hematocrit case. This faster decay can be explained by the larger shear-induced diffusion coefficient of $D_{RBC} = 38\ \mu\text{m}^2/\text{s}$. This agrees with the theoretical expectation that the shear-induced diffusion coefficient depends on the number of cell-cell collisions and thus on the cell concentration (101,103). The microparticles are still located in the cell-free layer in the center all along the main channel, as can be seen in Fig. 12, *c* and *d*. We can again calculate the fraction of antimarginated microparticles and obtain the fractions 0.145 at $x = 55\ \mu$m and 0.137 at $x = 158\ \mu$m. Also, when we compare the axial concentration of labeled red blood cells and microparticles in Fig. 13, *a* and *b*) to the case of lower hematocrit in Fig. 6, we see similar behavior in both cases.

When we investigate the influence of larger hematocrit on the system with bifurcation, we find that each cell-free layer in the system decreases with increasing hematocrit (results shown in Supporting Materials and Methods). At the end of the main channel, the cell-free layer still decreases, and the pronounced asymmetry of cell-free layers within the branches is present. The increase in concentration due to the apex of the bifurcation remains unaffected by larger hematocrit, as seen in Fig. 13, *c* and *d*. Because a certain number of cells or microparticles stacks at the apex of the bifurcation, the effect is not modified when more cells are added to the system. Especially, the absolute number of cells in the center region stays approximately the same for larger hematocrit.

Asymmetric bifurcations

We finally touch briefly on the subject of asymmetric bifurcations. For this, we keep the main channel radius $R_{ch} = 16\ \mu$m and the upper branch $R_{br} = 11.5\ \mu$m, as in Fig. 1 (*right*), and only vary the diameter of the lower branch. Two different simulations are done with radius $R^{low} = 8$ and $5.5\ \mu$m. Here, we focus on the total

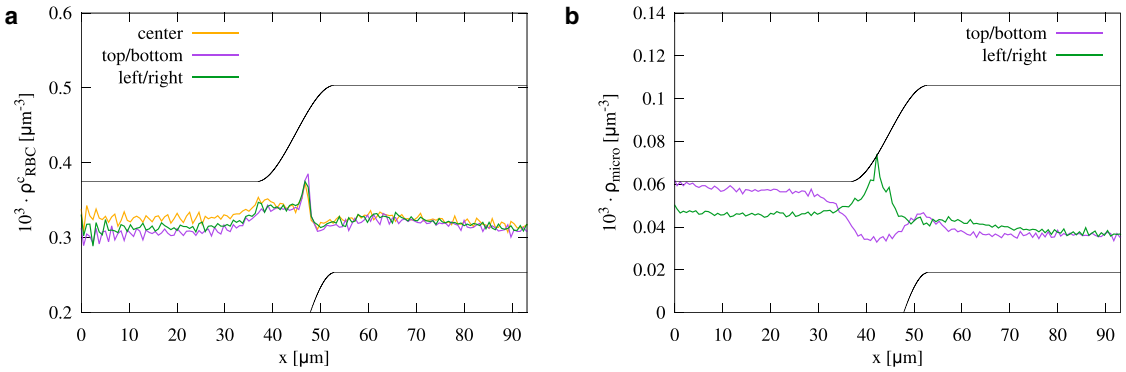

FIGURE 11 Axial concentration of (*a*) red blood cells and (*b*) microparticles distinguished regarding their initial position inside the cross section of the main channel. The peak in red blood cell concentration stems from the cells trapped at the apex of the bifurcation. The microparticles exhibit a similar peak when arriving left/right. However, for microparticles entering top/bottom, no peak occurs. To see this figure in color, go online.

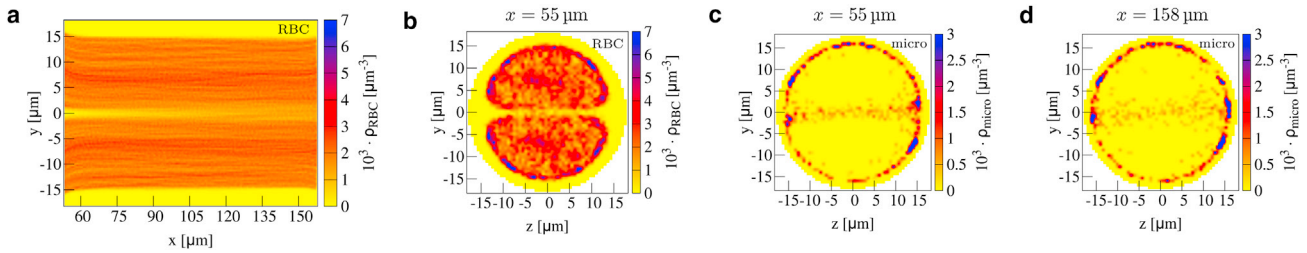

FIGURE 12 (*a*) 2D planar projection within the confluence for red blood cells along the main channel behind a confluence as in Fig. 3, but with larger hematocrit $Ht = 20\%$. (*b–d*) 2D cross-sectional profiles for (*b*) red blood cells and (*c* and *d*) microparticles in the main channel as in Fig. 4, but for larger hematocrit $Ht = 20\%$. To see this figure in color, go online.

concentration of red blood cells and microparticles within the two branches, as listed in Table 1.

The red blood cell concentration clearly differs between the upper and lower branch. The upper branch, being the one with the larger flow rate, receives clearly more cells than the lower branch. This effect is enhanced when the diameter and correspondingly the flow rate further decrease, as in the case of $R^{low} = 5.5$ μm. The fraction of concentration between lower and upper branch ρ^{low}/ρ^{up} changes from 0.77 to 0.67 when R^{low} is changed from 8 to 5.5 μm. We note that the total flow rate at the outflow of the system is the same in both simulations to match the flow rate at the entrance. As a consequence, the flow rate in the upper branch slightly differs in both simulations (the fractions of flow rates are 0.5 and 0.26, respectively). The asymmetric distribution of red blood cells qualitatively matches the Zweifach-Fung effect observed earlier (61,70,74,102) and can be attributed to the cell-free layer (102) combined with red blood cell deformability.

In contrast to the asymmetric red blood cell distribution, the microparticles are nearly evenly distributed to the daughter channels. Furthermore, the distribution is not affected by decreasing the diameter of the lower branch, the fraction in both cases being ~1.11. Because the stiff microparticles are located within the cell-free layer, the different flow rate does not affect their distribution. Although the lower branch is significantly smaller, the apex of the bifurcation and thus the separation line between the two branches are located near the center of the main channel by construction of the geometry. Thus,

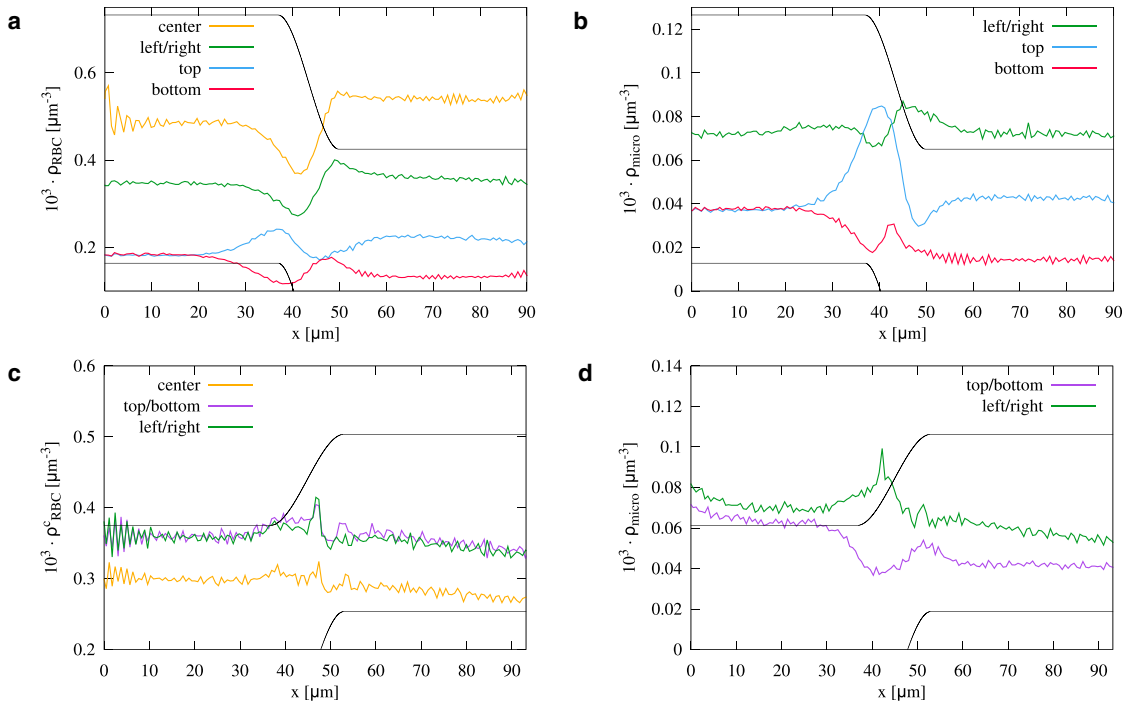

FIGURE 13 1D axial concentration of (*a* and *c*) red blood cells and (*b* and *d*) and microparticles flowing through a (*a* and *b*) confluence or (*c* and *d*) bifurcation with larger hematocrit $Ht = 20\%$ labeled by their radial position at the entrance. The larger hematocrit hardly affects the behavior of red blood cells and microparticles. To see this figure in color, go online.

TABLE 1 Concentration of Red Blood Cells and Microparticles in the Upper and Lower Channel of an Asymmetric Bifurcation with Radius 11 μm of the Upper Branch and R^{low} of the Lower Branch

R^{low}	ρ^{up}_{RBC}	ρ^{low}_{RBC}	ρ^{up}_{micro}	ρ^{low}_{micro}
8 μm	1.027	0.794	0.0711	0.0792
5.5 μm	1.005	0.674	0.0722	0.0806

Concentrations are given in 10^3 μm^{-3}.

arriving near the wall, only the microparticles located around the equator are drawn into the upper branch by the flow, whereas all other microparticles may be distributed equally into the branches. All in all, the microparticles exhibit a very similar concentration in both branches.

CONCLUSIONS

We used 3D IBM-LBM simulations with inflow/outflow boundary conditions to investigate a mixed suspension of red blood cells and stiff particles flowing through a vessel confluence as well as a vessel bifurcation. The stiff particles can be regarded as models for synthetic drug delivery agents or naturally occurring stiff cells such as platelets. In agreement with earlier studies, we observe and quantify the formation of a pronounced central cell-free layer behind the confluence of two vessels. We find that the central cell-free layer is very stable, being still observable even 100 μm after the confluence. As a consequence, we show that stiff particles at the confluence are strongly redistributed. Although all stiff particles arrive on a marginated position inside the well-known near-wall cell-free layer, while transversing the confluence, a significant fraction of them undergo antimargination, ending up trapped in the central cell-free layer near the channel center. This position is retained even longer than the 100 μm lifetime of the central cell-free layer itself. Calculating the fraction of antimarginated microparticles, we found that more than 13% of the particles are located around the center 100 μm behind a confluence. Under the assumption that at the succeeding confluence, this fraction of microparticles is still antimarginated, we estimate that after five confluences half of the initially completely marginated particles are now evenly distributed across the cross section of the channel. In contrast, a bifurcating geometry is found to not significantly influence the margination propensity of stiff particles. For the confluence, we also conducted in vivo measurements, which proved the relevance of antimargination of stiff microparticles in living mice.

In previous in vivo studies, platelets have been observed to be mainly located near the wall in arterioles (7,104) but not in venules, where the platelet concentration was rather continuous across vessel diameters. In a similar direction, the recent work of Casa et al. (75) found that thrombi were platelet-rich on the arterial but not on the venous side of the blood vessel network. Our findings may provide an explanation for these observations. On the arterial side, the microvascular network consists mainly of bifurcations from larger into smaller and smaller vessels, which according to our findings, do not significantly disturb the margination propensity of platelets. On the venous side, however, small channels frequently merge into larger ones. At such confluences, our results clearly demonstrated antimargination, i.e., the tendency of platelets to be forced into the center of the vessel. In a network with a cascade of confluences being only 400–1000 μm apart (2,4) the platelet margination near the channel wall will be further and further disturbed, ending up finally in a rather continuous concentration profile and thus explaining the experimental observations of (7,75).

SUPPORTING MATERIAL

Supporting Materials and Methods, thirteen figures, and three videos are available at http://www.biophysj.org/biophysj/supplemental/S0006-3495(18)30689-1.

AUTHOR CONTRIBUTIONS

C.B. performed the research, analyzed the data, and wrote the article. L.S. contributed to simulation tools. S.G. designed the research and wrote the article. A.K. performed image treatment and data analysis. C.W. designed and interpreted the research. L.K. and M.W.L. designed and performed the in vivo experiments.

ACKNOWLEDGMENTS

The authors thank the Gauss Centre for Supercomputing e.V. for providing computing time on the GCS Supercomputer SuperMUC at the Leibniz Supercomputing Centre. We gratefully acknowledge the Elite Study Program Biological Physics and the *Studienstiftung des deutschen Volkes*.

This work was supported by the Volkswagen Foundation.

REFERENCES

1. Popel, A. S., and P. C. Johnson. 2005. Microcirculation and Hemorheology. *Annu. Rev. Fluid Mech.* 37:43–69.
2. Pries, A. R., and T. W. Secomb. 2008. Chapter 1 blood flow in microvascular networks. *In* Microcirculation. Elsevier, pp. 3–36.
3. Misbah, C., and C. Wagner. 2013. Living fluids. *C. R. Phys.* 14:447–450.
4. Gompper, G., and D. A. Fedosov. 2016. Modeling microcirculatory blood flow: current state and future perspectives. *Wiley Interdiscip. Rev. Syst. Biol. Med.* 8:157–168.
5. Freund, J. B. 2014. Numerical simulation of flowing blood cells. *Annu. Rev. Fluid Mech.* 46:67–95.
6. Schmid-Schönbein, G. W., S. Usami, …, S. Chien. 1980. The interaction of leukocytes and erythrocytes in capillary and postcapillary vessels. *Microvasc. Res.* 19:45–70.
7. Woldhuis, B., G. J. Tangelder, …, R. S. Reneman. 1992. Concentration profile of blood platelets differs in arterioles and venules. *Am. J. Physiol.* 262:H1217–H1223.

8. Eckstein, E. C., A. W. Tilles, and F. J. Millero, III. 1988. Conditions for the occurrence of large near-wall excesses of small particles during blood flow. *Microvasc. Res.* 36:31–39.
9. Jain, A., and L. L. Munn. 2009. Determinants of leukocyte margination in rectangular microchannels. *PLoS One.* 4:e7104.
10. Charoenphol, P., R. B. Huang, and O. Eniola-Adefeso. 2010. Potential role of size and hemodynamics in the efficacy of vascular-targeted spherical drug carriers. *Biomaterials.* 31:1392–1402.
11. Chen, H., J. I. Angerer, …, A. Alexander-Katz. 2013. Hematocrit and flow rate regulate the adhesion of platelets to von Willebrand factor. *Biomicrofluidics.* 7:64113.
12. Namdee, K., A. J. Thompson, …, O. Eniola-Adefeso. 2013. Margination propensity of vascular-targeted spheres from blood flow in a microfluidic model of human microvessels. *Langmuir.* 29:2530–2535.
13. Wang, G., W. Mao, …, T. Sulchek. 2013. Stiffness dependent separation of cells in a microfluidic device. *PLoS One.* 8:e75901.
14. Lee, T. R., M. Choi, …, P. Decuzzi. 2013. On the near-wall accumulation of injectable particles in the microcirculation: smaller is not better. *Sci. Rep.* 3:2079.
15. Fitzgibbon, S., A. P. Spann, …, E. S. G. Shaqfeh. 2015. In vitro measurement of particle margination in the microchannel flow: effect of varying hematocrit. *Biophys. J.* 108:2601–2608.
16. D'Apolito, R., F. Taraballi, …, S. Guido. 2016. Microfluidic interactions between red blood cells and drug carriers by image analysis techniques. *Med. Eng. Phys.* 38:17–23.
17. D'Apolito, R., G. Tomaiuolo, …, S. Guido. 2015. Red blood cells affect the margination of microparticles in synthetic microcapillaries and intravital microcirculation as a function of their size and shape. *J. Control. Release.* 217:263–272.
18. Carboni, E. J., B. H. Bognet, …, A. W. K. Ma. 2016. Direct tracking of particles and quantification of margination in blood flow. *Biophys. J.* 111:1487–1495.
19. Fay, M. E., D. R. Myers, …, W. A. Lam. 2016. Cellular softening mediates leukocyte demargination and trafficking, thereby increasing clinical blood counts. *Proc. Natl. Acad. Sci. USA.* 113:1987–1992.
20. Migliorini, C., Y. Qian, …, L. L. Munn. 2002. Red blood cells augment leukocyte rolling in a virtual blood vessel. *Biophys. J.* 83:1834–1841.
21. Freund, J. B. 2007. Leukocyte margination in a model microvessel. *Phys. Fluids.* 19:023301.
22. Kumar, A., and M. D. Graham. 2011. Segregation by membrane rigidity in flowing binary suspensions of elastic capsules. *Phys. Rev. E Stat. Nonlin. Soft Matter Phys.* 84:066316.
23. Zhao, H., and E. S. G. Shaqfeh. 2011. Shear-induced platelet margination in a microchannel. *Phys. Rev. E Stat. Nonlin. Soft Matter Phys.* 83:061924.
24. Tan, J., A. Thomas, and Y. Liu. 2011. Influence of red blood cells on nanoparticle targeted delivery in microcirculation. *Soft Matter.* 8:1934–1946.
25. Zhao, H., E. S. G. Shaqfeh, and V. Narsimhan. 2012. Shear-induced particle migration and margination in a cellular suspension. *Phys. Fluids.* 24:011902.
26. Kumar, A., and M. D. Graham. 2012. Mechanism of margination in confined flows of blood and other multicomponent suspensions. *Phys. Rev. Lett.* 109:108102.
27. Fedosov, D. A., J. Fornleitner, and G. Gompper. 2012. Margination of white blood cells in microcapillary flow. *Phys. Rev. Lett.* 108:028104.
28. Freund, J. B., and B. Shapiro. 2012. Transport of particles by magnetic forces and cellular blood flow in a model microvessel. *Phys. Fluids.* 24:051904–051912.
29. Reasor, D. A., Jr., M. Mehrabadi, …, C. K. Aidun. 2013. Determination of critical parameters in platelet margination. *Ann. Biomed. Eng.* 41:238–249.
30. Kumar, A., R. G. H. Rivera, and M. D. Graham. 2014. Flow-induced segregation in confined multicomponent suspensions: effects of particle size and rigidity. *J. Fluid Mech.* 738:423–462.
31. Fedosov, D. A., and G. Gompper. 2014. White blood cell margination in microcirculation. *Soft Matter.* 10:2961–2970.
32. Müller, K., D. A. Fedosov, and G. Gompper. 2014. Margination of micro- and nano-particles in blood flow and its effect on drug delivery. *Sci. Rep.* 4:4871.
33. Vahidkhah, K., S. L. Diamond, and P. Bagchi. 2014. Platelet dynamics in three-dimensional simulation of whole blood. *Biophys. J.* 106:2529–2540.
34. Vahidkhah, K., and P. Bagchi. 2015. Microparticle shape effects on margination, near-wall dynamics and adhesion in a three-dimensional simulation of red blood cell suspension. *Soft Matter.* 11:2097–2109.
35. Henríquez Rivera, R. G., K. Sinha, and M. D. Graham. 2015. Margination regimes and drainage transition in confined multicomponent suspensions. *Phys. Rev. Lett.* 114:188101.
36. Müller, K., D. A. Fedosov, and G. Gompper. 2016. Understanding particle margination in blood flow: a step toward optimized drug delivery systems. *Med. Eng. Phys.* 38:2–10.
37. Gekle, S. 2016. Strongly accelerated margination of active particles in blood flow. *Biophys. J.* 110:514–520.
38. Krüger, T. 2016. Effect of tube diameter and capillary number on platelet margination and near-wall dynamics. *Rheol. Acta.* 55:511–526.
39. Mehrabadi, M., D. N. Ku, and C. K. Aidun. 2016. Effects of shear rate, confinement, and particle parameters on margination in blood flow. *Phys. Rev. E.* 93:023109.
40. Spann, A. P., J. E. Campbell, …, E. S. G. Shaqfeh. 2016. The effect of hematocrit on platelet adhesion: experiments and simulations. *Biophys. J.* 111:577–588.
41. Guckenberger, A., and S. Gekle. 2018. A boundary integral method with volume-changing objects for ultrasound-triggered margination of microbubbles. *J. Fluid Mech.* 836:952–997.
42. Tokarev, A. A., A. A. Butylin, …, F. I. Ataullakhanov. 2011. Finite platelet size could be responsible for platelet margination effect. *Biophys. J.* 101:1835–1843.
43. Crowl, L., and A. L. Fogelson. 2011. Analysis of mechanisms for platelet near-wall excess under arterial blood flow conditions. *J. Fluid Mech.* 676:348–375.
44. Henríquez Rivera, R. G., X. Zhang, and M. D. Graham. 2016. Mechanistic theory of margination and flow-induced segregation in confined multicomponent suspensions: simple shear and poiseuille flows. *Phys. Rev. Fluids.* 1:060501.
45. Qi, Q. M., and E. S. G. Shaqfeh. 2017. Theory to predict particle migration and margination in the pressure-driven channel flow of blood. *Phys. Rev. Fluids.* 2:093102.
46. Qi, Q. M., and E. S. Shaqfeh. 2018. Time-dependent particle migration and margination in the pressure-driven channel flow of blood. *Phys. Rev. Fluids.* 3:034302.
47. Mountrakis, L., E. Lorenz, and A. G. Hoekstra. 2013. Where do the platelets go? A simulation study of fully resolved blood flow through aneurysmal vessels. *Interface Focus.* 3:20120089.
48. Wu, W.-T., Y. Li, …, J. F. Antaki. 2017. Numerical simulation of red blood cell-induced platelet transport in saccular aneurysms. *Appl. Sci. (Basel).* 7:484.
49. Zhao, R., J. N. Marhefka, …, J. F. Antaki. 2008. Micro-flow visualization of red blood cell-enhanced platelet concentration at sudden expansion. *Ann. Biomed. Eng.* 36:1130–1141.
50. Faivre, M., M. Abkarian, …, H. A. Stone. 2006. Geometrical focusing of cells in a microfluidic device: an approach to separate blood plasma. *Biorheology.* 43:147–159.
51. Fujiwara, H., T. Ishikawa, …, T. Yamaguchi. 2009. Red blood cell motions in high-hematocrit blood flowing through a stenosed microchannel. *J. Biomech.* 42:838–843.

52. Vahidkhah, K., P. Balogh, and P. Bagchi. 2016. Flow of red blood cells in stenosed microvessels. *Sci. Rep.* 6:28194.

53. Wang, W., T. G. Diacovo, …, M. R. King. 2013. Simulation of platelet, thrombus and erythrocyte hydrodynamic interactions in a 3D arteriole with in vivo comparison. *PLoS One.* 8:e76949.

54. Skorczewski, T., L. C. Erickson, and A. L. Fogelson. 2013. Platelet motion near a vessel wall or thrombus surface in two-dimensional whole blood simulations. *Biophys. J.* 104:1764–1772.

55. Yazdani, A., and G. E. Karniadakis. 2016. Sub-cellular modeling of platelet transport in blood flow through microchannels with constriction. *Soft Matter.* 12:4339–4351.

56. Bächer, C., L. Schrack, and S. Gekle. 2017. Clustering of microscopic particles in constricted blood flow. *Phys. Rev. Fluids.* 2:013102.

57. Li, X., A. S. Popel, and G. E. Karniadakis. 2012. Blood-plasma separation in Y-shaped bifurcating microfluidic channels: a dissipative particle dynamics simulation study. *Phys. Biol.* 9:026010.

58. Tripathi, S., Y. B. V. Kumar, …, A. Agrawal. 2015. Passive blood plasma separation at the microscale: a review of design principles and microdevices. *J. Micromech. Microeng.* 25:083001.

59. Svanes, K., and B. Zweifach. 1968. Variations in small blood vessel hematocrits produced in hypothermic rats by micro-occlusion. *Microvasc. Res.* 1:210–220.

60. Fung, Y. C. 1973. Stochastic flow in capillary blood vessels. *Microvasc. Res.* 5:34–48.

61. Pries, A. R., K. Ley, …, P. Gaehtgens. 1989. Red cell distribution at microvascular bifurcations. *Microvasc. Res.* 38:81–101.

62. Pries, A. R., T. W. Secomb, and P. Gaehtgens. 1996. Biophysical aspects of blood flow in the microvasculature. *Cardiovasc. Res.* 32:654–667.

63. Shen, Z., G. Coupier, …, T. Podgorski. 2016. Inversion of hematocrit partition at microfluidic bifurcations. *Microvasc. Res.* 105:40–46.

64. Leble, V., R. Lima, …, T. Yamaguchi. 2011. Asymmetry of red blood cell motions in a microchannel with a diverging and converging bifurcation. *Biomicrofluidics.* 5:44120–4412015.

65. Wang, T., U. Rongin, and Z. Xing. 2016. A micro-scale simulation of red blood cell passage through symmetric and asymmetric bifurcated vessels. *Sci. Rep.* 6:20262.

66. Barber, J. O., J. M. Restrepo, and T. W. Secomb. 2011. Simulated red blood cell motion in microvessel bifurcations: effects of cell-cell interactions on cell partitioning. *Cardiovasc. Eng. Technol.* 2:349–360.

67. Ng, Y. C., B. Namgung, …, S. Kim. 2016. Symmetry recovery of cell-free layer after bifurcations of small arterioles in reduced flow conditions: effect of RBC aggregation. *Am. J. Physiol. Heart Circ. Physiol.* 311:H487–H497.

68. Namgung, B., Y. C. Ng, …, S. Kim. 2017. Near-wall migration dynamics of erythrocytes in vivo: effects of cell deformability and arteriolar bifurcation. *Front. Physiol.* 8:963.

69. Balogh, P., and P. Bagchi. 2017. Direct numerical simulation of cellular-scale blood flow in 3D microvascular networks. *Biophys. J.* 113:2815–2826.

70. Balogh, P., and P. Bagchi. 2017. A computational approach to modeling cellular-scale blood flow in complex geometry. *J. Comput. Phys.* 334:280–307.

71. Balogh, P., and P. Bagchi. 2018. Analysis of red blood cell partitioning at bifurcations in simulated microvascular networks. *Phys. Fluids.* 30:051902–051917.

72. Yang, X., O. Forouzan, …, S. S. Shevkoplyas. 2011. Traffic of leukocytes in microfluidic channels with rectangular and rounded cross-sections. *Lab Chip.* 11:3231–3240.

73. Sun, C., and L. L. Munn. 2008. Lattice Boltzmann simulation of blood flow in digitized vessel networks. *Comput. Math. Appl.* 55:1594–1600.

74. Lykov, K., X. Li, …, G. E. Karniadakis. 2015. Inflow/outflow boundary conditions for particle-based blood flow simulations: application to arterial bifurcations and trees. *PLoS Comput. Biol.* 11:e1004410.

75. Casa, L. D., D. H. Deaton, and D. N. Ku. 2015. Role of high shear rate in thrombosis. *J. Vasc. Surg.* 61:1068–1080.

76. Succi, S. 2001. The Lattice Boltzmann Equation: For Fluid Dynamics and Beyond. Oxford university press, Oxford, UK.

77. Dünweg, B., and A. J. Ladd. 2008. Lattice Boltzmann simulations of soft matter systems. *In* Advanced Computer Simulation Approaches for Soft Matter Sciences III. Springer, pp. 89–166.

78. Aidun, C. K., and J. R. Clausen. 2010. Lattice-Boltzmann method for complex flows. *Annu. Rev. Fluid Mech.* 42:439–472.

79. Limbach, H., A. Arnold, …, C. Holm. 2006. ESPResSo—an extensible simulation package for research on soft matter systems. *Comput. Phys. Commun.* 174:704–727.

80. Roehm, D., and A. Arnold. 2012. Lattice Boltzmann simulations on GPUs with ESPResSo. *Eur. Phys. J. Spec. Top.* 210:89–100.

81. Arnold, A., O. Lenz, …, C. Holm. 2013. Espresso 3.1: Molecular dynamics software for coarse-grained models. *In* Meshfree methods for partial differential equations VI. Springer, pp. 1–23.

82. Peskin, C. S. 2002. The immersed boundary method. *Acta Numer.* 11:479–517.

83. Mittal, R., and G. Iaccarino. 2005. Immersed boundary methods. *Annu. Rev. Fluid Mech.* 37:239–261.

84. Barthès-Biesel, D. 2011. Modeling the motion of capsules in flow. *Curr. Opin. Colloid Interface Sci.* 16:3–12.

85. Daddi-Moussa-Ider, A., A. Guckenberger, and S. Gekle. 2016. Long-lived anomalous thermal diffusion induced by elastic cell membranes on nearby particles. *Phys. Rev. E.* 93:012612.

86. Guckenberger, A., M. P. Schraml, …, S. Gekle. 2016. On the bending algorithms for soft objects in flows. *Comput. Phys. Commun.* 207:1–23.

87. Guckenberger, A., and S. Gekle. 2017. Theory and algorithms to compute Helfrich bending forces: a review. *J. Phys. Condens. Matter.* 29:203001.

88. Fedosov, D. A., M. Peltomäki, and G. Gompper. 2014. Deformation and dynamics of red blood cells in flow through cylindrical microchannels. *Soft Matter.* 10:4258–4267.

89. Guckenberger, A., A. Kihm, …, S. Gekle. 2018. Numerical-experimental observation of shape bistability of red blood cells flowing in a microchannel. *Soft Matter.* 14:2032–2043.

90. Jeffery, G. B. 1922. The motion of ellipsoidal particles immersed in a viscous fluid. *Proc. R. Soc. Lond., A Contain. Pap. Math. Phys. Character.* 102:161–179.

91. Yang, S., A. Ündar, and J. D. Zahn. 2006. A microfluidic device for continuous, real time blood plasma separation. *Lab Chip.* 6:871–880.

92. Laschke, M. W., and M. D. Menger. 2016. The dorsal skinfold chamber: a versatile tool for preclinical research in tissue engineering and regenerative medicine. *Eur. Cell. Mater.* 32:202–215.

93. Laschke, M. W., B. Vollmar, and M. D. Menger. 2011. The dorsal skinfold chamber: window into the dynamic interaction of biomaterials with their surrounding host tissue. *Eur. Cell. Mater.* 22:147–164, discussion 164–167.

94. Brust, M., O. Aouane, …, C. Wagner. 2014. The plasma protein fibrinogen stabilizes clusters of red blood cells in microcapillary flows. *Sci. Rep.* 4:4348.

95. Fedosov, D. A., B. Caswell, …, G. E. Karniadakis. 2010. Blood flow and cell-free layer in microvessels. *Microcirculation.* 17:615–628.

96. Freund, J. B., and M. M. Orescanin. 2011. Cellular flow in a small blood vessel. *J. Fluid Mech.* 671:466–490.

97. Katanov, D., G. Gompper, and D. A. Fedosov. 2015. Microvascular blood flow resistance: role of red blood cell migration and dispersion. *Microvasc. Res.* 99:57–66.

98. Turitto, V. T., and H. R. Baumgartner. 1975. Platelet deposition on subendothelium exposed to flowing blood: mathematical analysis of physical parameters. *Trans. Am. Soc. Artif. Intern. Organs.* 21:593–601.

99. Goldsmith, H., and J. Marlow. 1979. Flow behavior of erythrocytes. II. Particle motions in concentrated suspensions of ghost cells. *J. Colloid Interface Sci.* 71:383–407.

100. Kumar, A., and M. D. Graham. 2012. Margination and segregation in confined flows of blood and other multicomponent suspensions. *Soft Matter.* 8:10536–10548.

101. Grandchamp, X., G. Coupier, …, T. Podgorski. 2013. Lift and down-gradient shear-induced diffusion in red blood cell suspensions. *Phys. Rev. Lett.* 110:108101.

102. Secomb, T. W. 1995. Mechanics of blood flow in the microcirculation. *Symp. Soc. Exp. Biol.* 49:305–321.

103. Da Cunha, F. R., and E. J. Hinch. 1996. Shear-induced dispersion in a dilute suspension of rough spheres. *J. Fluid Mech.* 309:211–223.

104. Tangelder, G. J., H. C. Teirlinck, …, R. S. Reneman. 1985. Distribution of blood platelets flowing in arterioles. *Am. J. Physiol.* 248:H318–H323.

Biophysical Journal, Volume *115*

Supplemental Information

Antimargination of Microparticles and Platelets in the Vicinity of Branching Vessels

Christian Bächer, Alexander Kihm, Lukas Schrack, Lars Kaestner, Matthias W. Laschke, Christian Wagner, and Stephan Gekle

Supplemental Information - Anti-margination of microparticles and platelets in the vicinity of branching vessels

Christian Bächer[1], A. Kihm[2], L. Schrack[1,3], L. Kaestner[4], M.W. Laschke[5], C. Wagner[2], and S. Gekle[1]

[1]Biofluid Simulation and Modeling, Theoretische Physik, Universität Bayreuth, Bayreuth, Germany
[2]Experimental Physics, Saarland University, Saarbrücken, Germany
[3]Institute for Theoretical Physics, University of Innsbruck, Innsbruck, Austria
[4]Institute for Molecular Cell Biology, Research Centre for Molecular Imaging and Screening, Center for Molecular Signaling (PZMS), Medical Faculty, Saarland University, Homburg/Saar, Germany
[5]Institute for Clinical & Experimental Surgery, Saarland University, Homburg/Saar, Germany

Inflow: full margination and constant particle number

In figure S1 we show the state of complete margination at the entrance of a bifurcating channel and a confluence, respectively. The cross-sectional concentrations show the red blood cells accumulated around the channel center and the microparticles close to the wall.

Figure S2 shows that after a short transient time the implemented particle inflow/outflow leads to a constant number of red blood cells and microparticles in the system.

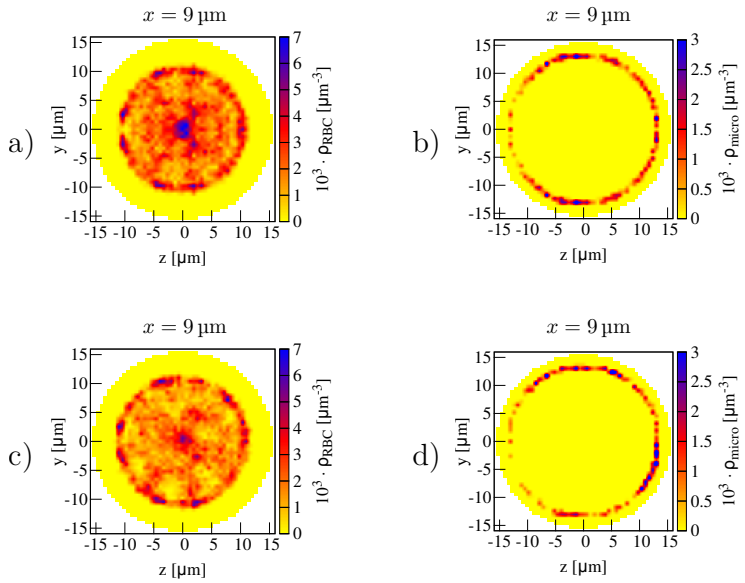

Figure S1: At the entrance of the confluence system a),b) and the bifurcation system c),d) we have a state of full margination: the red blood cells a),c) are located in the channel center, the microparticles b),d) near the wall.

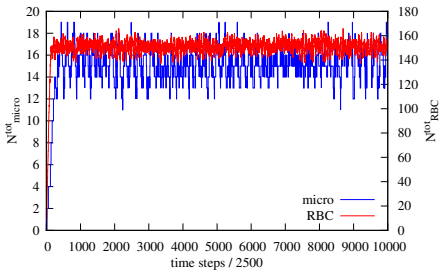

Figure S2: Total number of RBCs and microparticles within the confluence system depending on the simulation time. Both numbers fluctuate around a constant value after initial filling of the system.

Concentration profiles of tracer particles

In order to model the behavior of red blood cells and microparticles we use passive point particles as tracers flowing with the intrinsic velocity profile (1). We first start with the confluence. Homogeneously distributed particles exhibit a similar concentration profile as the red blood cells. As a consequence, red blood cell behavior can be explained by the intrinsic velocity profile. Doing the same calculations for tracers in the different regions resemble the labeled red blood cells. It also fits the concentration profiles for the microparticles.

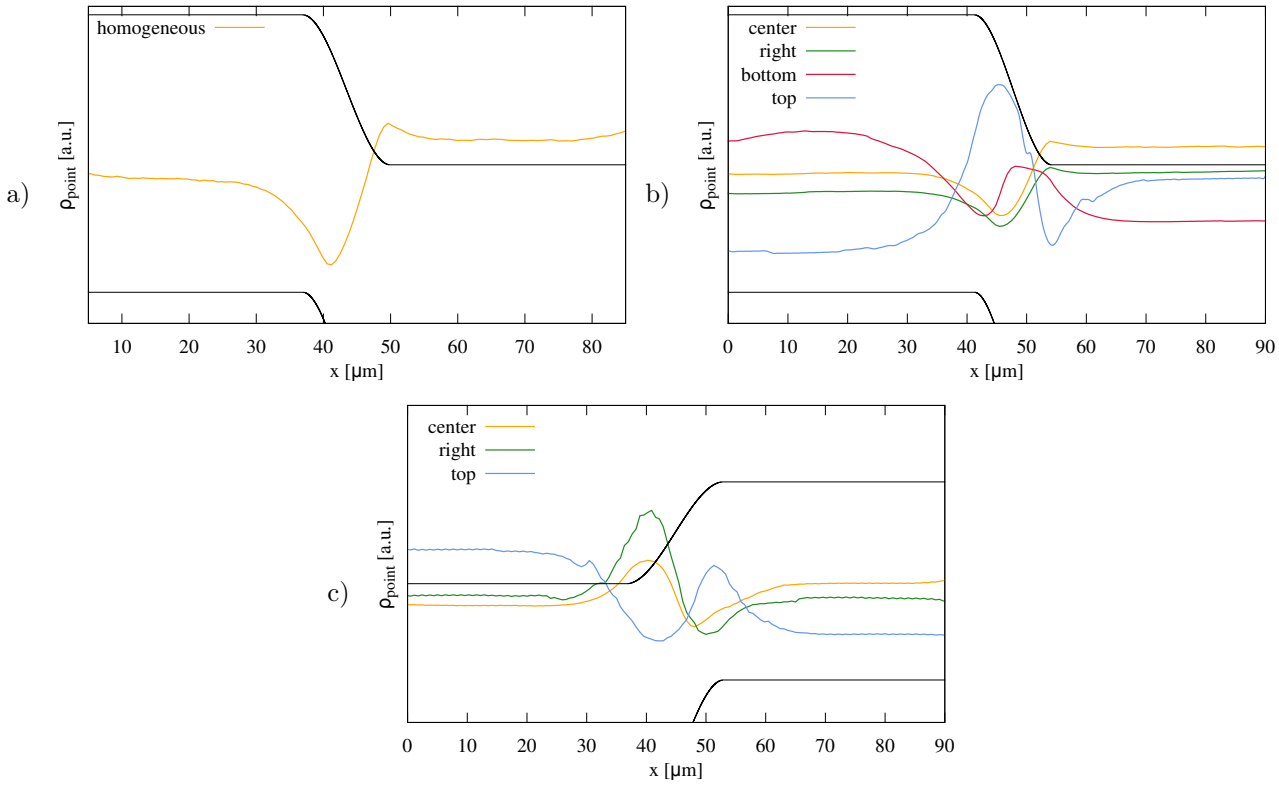

Figure S3: Concentration of a) homogeneously distributed tracer particles and b) tracer particles flowing in the distinct regions at system entrance within the confluence. c) Tracer particles flowing in the distinct regions at system entrance within the diverging bifurcation. These figures are compared to cell and particle concentration in figure 6, 11 and 13 in the main text.

In the diverging bifurcation starting at top the concentration profile of the point particles matches that of the microparticles quite well. Also the point particles located right reproduce microparticle behavior. We note that starting point particles top or bottom and left or right results in the same concentration due to symmetry. Red

blood cell behavior is also similar to that of point particles, except the peak at the bifurcation apex. The differences are effects due to the finite size and deformability of red blood cells.

Shear-induced diffusion

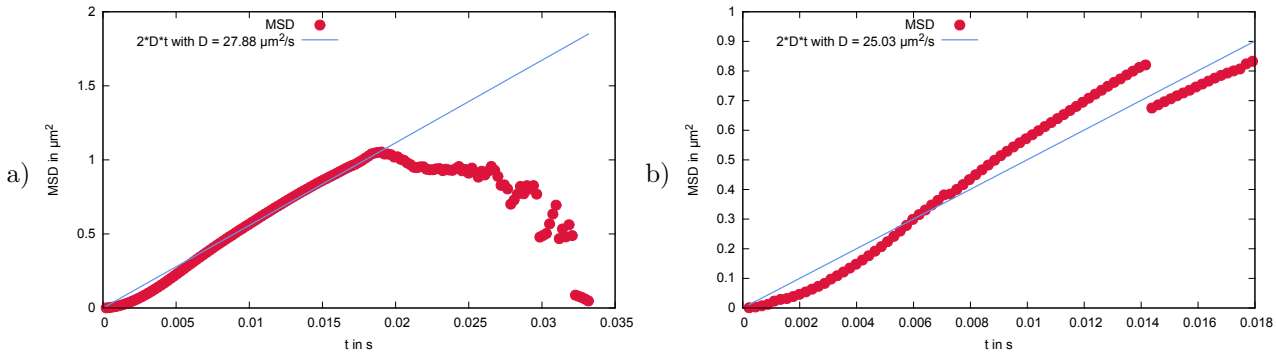

Figure S4: Mean square displacement over time for a) red blood cells and b) microparticles located near the center behind a confluence. By modeling the theoretical expectation we can extract a shear-induced diffusion coefficient.

Larger hematocrit

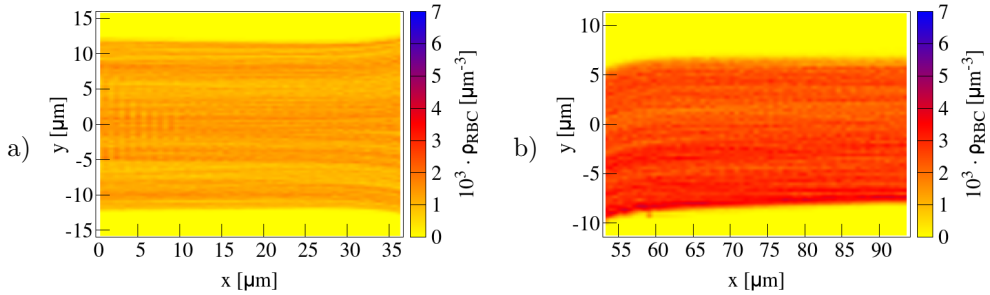

Figure S5: 2D planar projection for red blood cells along the a) main channel and b) branches of the bifurcation with larger hematocrit $Ht = 20\%$. The cell-free layer decreases, but the behavior is qualitatively unchanged.

Anti-margination of platelet-shaped microparticles

In the main text we focus on spherical microparticles. Here, we show additional results for oblate spheroids – a geometry that mimicks more closely that of real platelets. The platelets have a diameter of 3.9 μm along the two long axes and 2.3 μm along the small axis and are illustrated in figure S6. Similar to the spherical particles of the main text, about 14% of the spheroidal microparticles are anti-marginated directly behind the confluence.

Narrow confluence

In figure S7 we investigate the influence of the main vessel diameter. We perform simulations with radius 22.8 μm and 14.3 μm of the main vessel, but with the same branch properties as in figure 1 a) of the main text. In figure S7 a) the red blood cell concentration shows a more stable central cell-free layer for a wider vessel. In case of a narrow vessel the central cell-free layer vanishes more quickly (figure S7 b). Correspondingly, the microparticles stay close

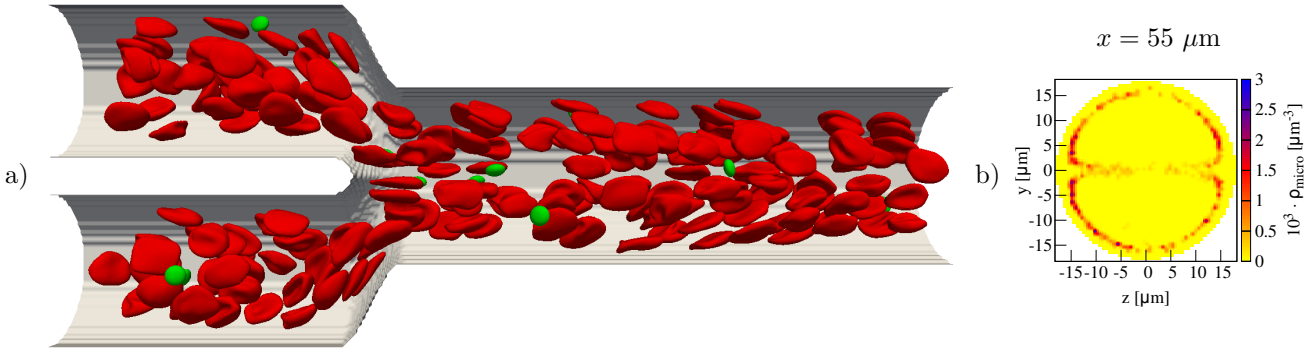

Figure S6: (a) Simulation of microparticles with a platelet-like oblate shape flowing through a confluence. (b) Similar to the spherical microparticles of the main text, these particles also undergo anti-margination.

to the center in the wider vessel (figure S7 c) and marginate faster within the narrow main vessel (figure S7 d). Both observations can be explained by the shear-induced diffusion coefficient depending on the local cell concentration, which increases with narrowing main vessel for the same inflow. Indeed, the red blood cell shear-induced diffusion coefficient decreases in figure S7 a) to 15.5 μm^2/s and increases in figure S7 b) to 45.4 μm^2/s.

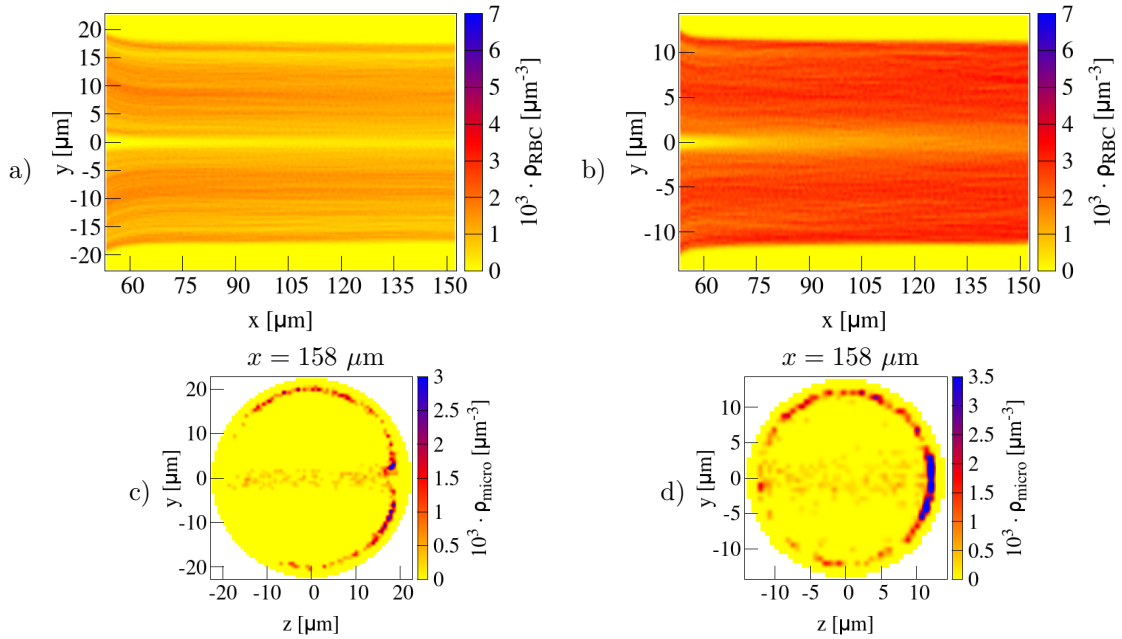

Figure S7: a),b) Red blood cell distribuition and c),d) cross-sectional microparticle concentration 100 μm behind a confluence with main vessel radius of a),c) 22.8 μm and b),d) 14.3 μm. While a wider vessel leads to a more stable central cell-free layer a narrow vessel causes the cell-free layer to smear out faster. Correspondingly, in case of a narrower main channel margination of microparticles takes place faster.

Validation of the used IBM-LBM algorithm

In the following, we summarize and extend the validation for our Immersed Boundary method (IBM) and Lattice-Boltzmann method (LBM). In ref. (2) the calculation of shear and bending forces has been validated for a capsule in shear flow. In ref. (3) the hematocrit profile for tube flow and plane-Poiseuille flow has been shown to agree with previous, established studies. Furthermore, the stability of the stiff spherical particles used has been demonstrated and the flow profile past a sphere has been compared favorably to the analytical solution.

In addition, we here calculate the Stokes drag $1/(6\pi\eta a)$ that relates the force on a sphere of radius a to its velocity in a suspending fluid of viscosity η for a sphere with two different particle resolutions in figure S8. We performed simulations with the resolution used in the main text (81 nodes of the inner stiff grid) and an increased resolution (485 nodes of the inner grid). We note that for the former the number of fluid nodes per particle does not change compared to the main text. Both resolutions show good agreement with the theoretical prediction and convergence to the theory for increasing grid resolution.

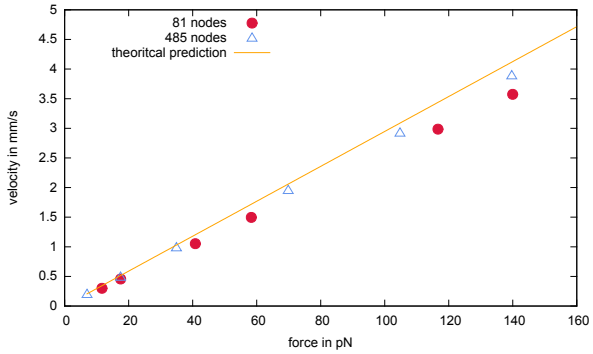

Figure S8: Velocity of a spherical particle pulled through a fluid with a given force. Simulations with two different particle resolutions are compared to the theoretical prediction given by the Stokes drag. The resolution given in the legend denotes the node number of the stiff inner grid.

In order to provide another quantitative validation of stiff particle behavior we simulate a spheroid with aspect ratio $\epsilon = 3$ subjected to shear flow, as sketched in figure S9 a). Ref. (4) provides an analytical solution for the spheroid inclination angle θ over time t

$$\theta(t) = \tan^{-1}\left(\epsilon \tan\left(\frac{t\dot{\gamma}}{\epsilon + \frac{1}{\epsilon}}\right)\right), \tag{S1}$$

with $\dot{\gamma}$ being the shear rate. In figure S9 b) we compare our numerical results (2562 nodes and 5120 triangles for the outer membrane of the spheroid) to the theoretical prediction and find very good agreement.

In order to validate the red blood cell behavior, we present a detailed investigation of a single red blood cell flowing through a cylindrical channel. In figure S10 we show the red blood cell shape obtained for a confinement - effective red blood cell diameter divided by the channel diameter - of 0.55, which can directly be compared to literature data in figure 1 of Fedosov et al. (5). From left to right we increased the dimensionless shear $\dot{\gamma}^* = \bar{\dot{\gamma}}\tau$ with the averaged shear rate $\bar{\dot{\gamma}}$ defined by the averaged velocity over the channel diameter and τ the relaxation time of a red blood cell. Since in this setup the focus is on the single cell behavior we performed our simulations with a membrane mesh resolution of 5120 triangles. With increasing velocity we first observe a tumbling discocyte, a tank-treading slipper, and eventually a croissant. The shapes are in very good agreement with the shapes shown in figure 1 of ref. (5).

Furthermore, we compare the single cell behavior for different resolutions of the red blood cell mesh with simulations using the Boundary Integral method (BIM) in a rectangular channel of cross-section 10 μm x 12 μm in figure S11. The BIM simulations are part of an extensive study on single cell behavior in rectangular channels which demonstrated quantitative agreement with detailed experiments (6). The presently used LBM-IBM method leads to the same shapes as the more sophisticated BIM simulations.

We further validate our method considering the red blood cell behavior in a setup strongly related to those of the main text: we investigate the Zweifach-Fung effect and compare the results with literature data for a bifurcation

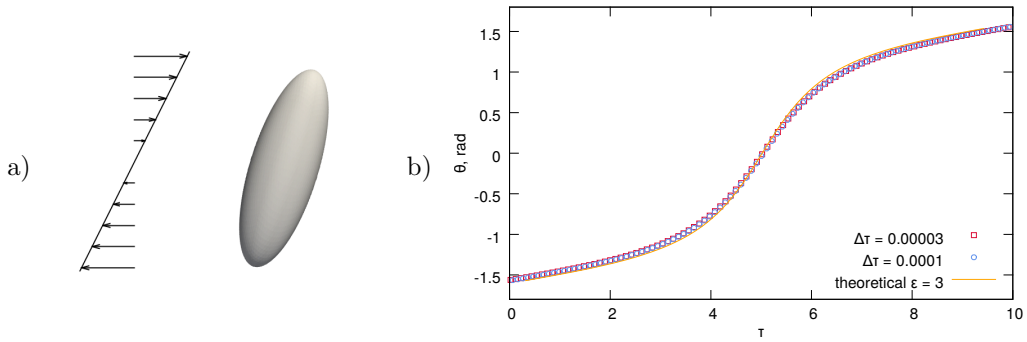

Figure S9: a) A rigid spheroid subjected to a shear flow. b) The orientation angle of the spheroid $\theta(\tau)$ over time $\tau = \dot{\gamma}t$ for simulations with different time steps compared to the analytical solution of ref. (4).

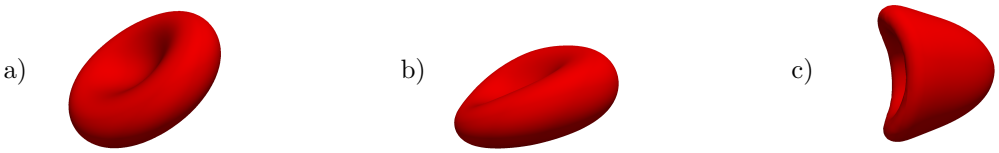

Figure S10: Red blood cell shapes in a cylinder for different flow rates obtained with LBM-IBM simulations. The confinement is 0.55.We observe a) a tumbling discocyte for a shear rate $\dot{\gamma}^* = 5$, b) a slipper for $\dot{\gamma}^* = 22.5$ and c) a croissant for $\dot{\gamma}^* = 60$. These shapes are in very good agreement with the shapes shown in figure 1 of ref. (5) for a confinement of 0.58 and $\dot{\gamma}^* = 5$, $\dot{\gamma}^* = 24.8$, and $\dot{\gamma}^* = 59.6$, respectively, that are obtained using Dissipative Particle Dynamics (5).

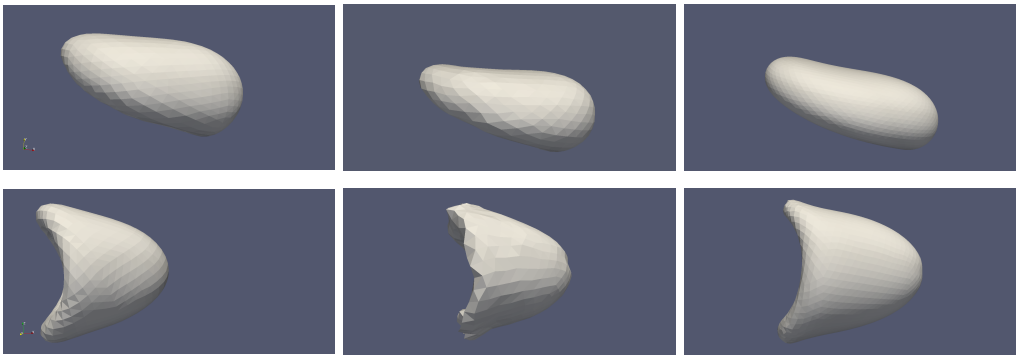

Figure S11: Single red blood cell in a rectangular channel with cross-section 10 μm x 12 μm simulated with the Boundary Integral method from (6), LBM-IBM with 1280 triangles and LBM-IBM 5120 triangles (from left to right). For a centroid velocity of 0.5 mm/s (top) a tank-treading slipper shape is observed and for 1.5 mm/s (bottom) a croissant shape.

of a vessel into two daughter vessels followed by a confluence, as sketched in figure S12 a). In contrast to the main text, here we use periodic boundary conditions. We construct our setup in a way that the cross-sections of the cylindrical branches match with the setup consisting of rectangular vessels of ref. (7), namely the main branch with radius 6.84 μm, the bottom branch with 5.86 μm, and the top branch varied in the range of 3.26 μm to 5.35 μm. We simulate a suspension of 50 red blood cells with a membrane mesh consisting of 642 nodes and 1280 triangles being the same as in the main text. The fluid grid is chosen such that the number of fluid nodes per cell is also the same as in the main text. With varying flow rate ratio between the bottom branch and the main branch (achieved by varying the diameter of the top branch) a disproportional partitioning of the red blood cells takes place, known as the Zweifach-Fung effect (7–9). In order to quantify this behavior in simulations we calculate the fraction of

the flow rate in the bottom branch Q_{bot} and in the main branch Q_m without any cells present. This is done by integrating the axial velocity v_x over the cross-section C of the branch

$$Q_{\mathrm{m}} = \int_C v_x^{\mathrm{m}} \mathrm{d}A, \quad Q_{\mathrm{bot}} = \int_C v_x^{\mathrm{bot}} \mathrm{d}A. \tag{S2}$$

As a measure for the red blood cell flux we calculate the number of red blood cells per time $\dot{N}(t)$ passing through the mid-plane of main branch and bottom branch, respectively, and average over all T time steps

$$n = \langle \dot{N}(t) \rangle_t = \frac{\sum_{i=1}^{T} \dot{N}(t_i) \Delta t}{\sum_{i=1}^{T} \Delta t}. \tag{S3}$$

We compare the fraction of red blood cell flux in bottom and main branch $n_{\mathrm{bot}}/n_{\mathrm{m}}$ to data from the literature in figure S12 b). As done in ref. (7) we compare our results with experimental values from Pries et al. (8) and Yang et al. (10) as well as with the numerical values from Balogh and Bagchi (7). Overall, we find very good agreement and our simulations show the expected half-sigmoidal variation collapsing with literature data over a wide range of flow rate fractions. We note that varying the overall velocity does not affect the results in figure S12.

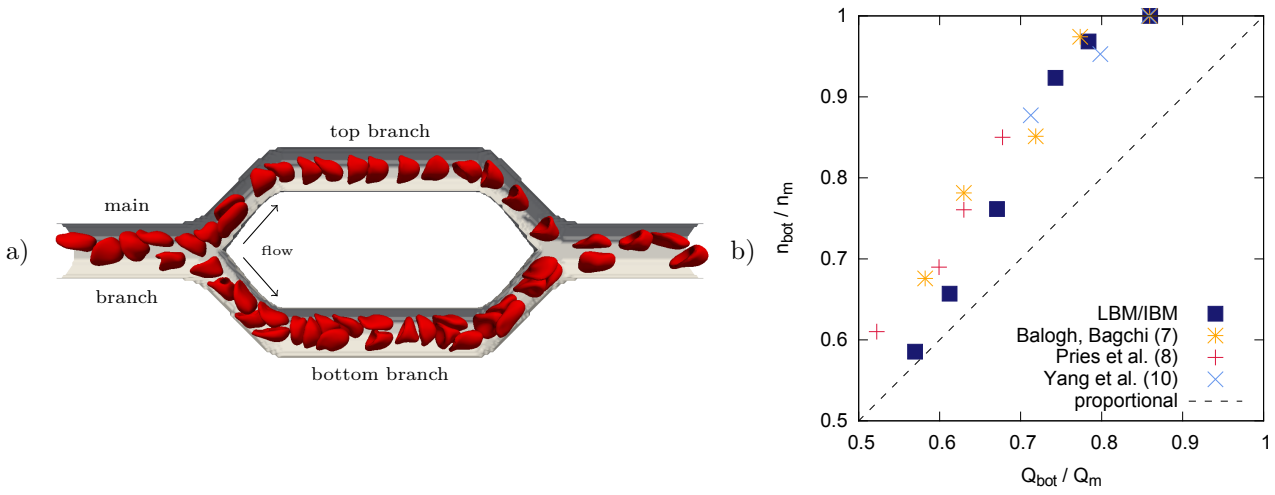

Figure S12: Red blood cells flowing through a bifurcation followed by a confluence. a) Simulation snapshot of one setup: main branch with radius 6.84 μm, bottom branch with radius 5.86 μm, and top branch with radius 5.35 μm. b) Fraction of cells flowing through the bottom branch n_{bot} and the main branch n_{m} depending on the fraction of flow rate in bottom Q_{bot} and main branch Q_{m}. Despite some deviations at low flow rate fraction our simulations lead to the expected half-sigmoidal dependency and match literature data at large fractions.

Next, in order to prove mesh insensitivity we reduced the resolution of the membrane mesh of the red blood cells to 258 nodes and 512 triangles and the resolution of the stiff particles to 66 nodes and 128 triangles. In the same way the fluid mesh changes from 288x110x58 to 200x82x42. The red blood cell distribution behind a confluence and the cross-sectional microparticle concentration are compared to the results of the manuscript in figure S13 a),b) and d),e), respectively. The results are in very good agreement. Small discrepancies may be caused by slightly different inflow concentrations.

Finally, in figure S13 c), f) we provide evidence that the repulsion force among the cells and particles does not affect our results. For this, we show the red blood cell distribution behind a confluence (corresponding to figure S13 b) and the cross-sectional microparticle concentration (corresponding to figure S13 e) for a simulation without repulsion force. We observe very similar behavior and are thus able to conclude that our main results are robust with respect to the repulsion force.

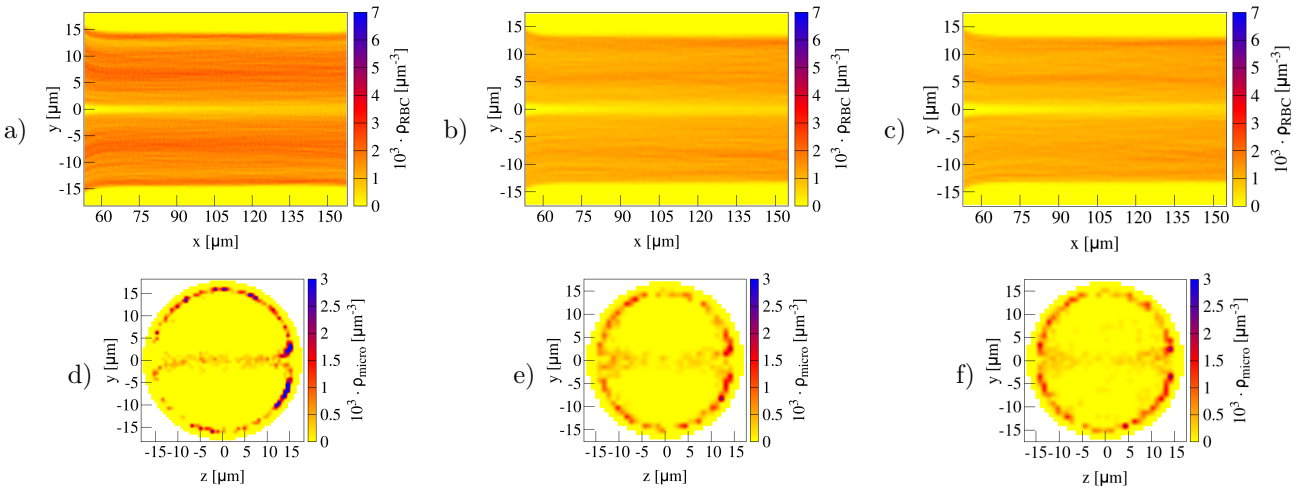

Figure S13: The main results for different mesh resolutions: The cell free-layer in a), b), c) and the microparticle anti-margination in d), e), f). a),d) resolution used in the main text (RBC: 1280, microparticle: 320, fluid: 288x110x58) and b), c), e), f) decreased resolution (RBC: 512, microparticle: 128, fluid: 200x82x42). Both resolutions lead to similar results for central cell free layer stability (in a) and b)) and fraction of anti-marginated microparticles (d) 15.8% and e) 16.2%). In figure c) and f) we provide evidence that without any repulsive force between cells, particles, and the vessel wall our main results do not change (16.7% antimarginated microparticles in f). Figures a) and d) are from the main text.

Taken together, our LBM-IBM method gives accurate results for stiff particles and red blood cells in simple tube flow, but also within a more complex system such as a bifurcation followed by a confluence. We provided evidence that neither the resolution of cell membrane mesh nor the fluid mesh nor the introduced repulsive force for additional stability affect our main results and conclusions.

References

[1] Bächer, C., L. Schrack, and S. Gekle, 2017. Clustering of Microscopic Particles in Constricted Blood Flow. Physical Review Fluids 2:013102.

[2] Guckenberger, A., M. P. Schraml, P. G. Chen, M. Leonetti, and S. Gekle, 2016. On the bending algorithms for soft objects in flows. Computer Physics Communications 207:1–23.

[3] Gekle, S., 2016. Strongly Accelerated Margination of Active Particles in Blood Flow. Biophysical Journal 110:514 – 520.

[4] Jeffery, G. B., 1922. The motion of ellipsoidal particles immersed in a viscous fluid. Proc. R. Soc. Lond. A 102:161–179.

[5] Fedosov, D. A., M. Peltomäki, and G. Gompper, 2014. Deformation and dynamics of red blood cells in flow through cylindrical microchannels. Soft matter 10:4258–4267.

[6] Guckenberger, A., A. Kihm, T. John, C. Wagner, and S. Gekle, 2018. Numerical-experimental observation of shape bistability of red blood cells flowing in a microchannel. Soft Matter 14:2032–2043.

[7] Balogh, P., and P. Bagchi, 2017. A Computational Approach to Modeling Cellular-Scale Blood Flow in Complex Geometry. Journal of Computational Physics 334:280–307.

[8] Pries, A., K. Ley, M. Claassen, and P. Gaehtgens, 1989. Red cell distribution at microvascular bifurcations. Microvascular research 38:81–101.

[9] Secomb, T. W., 2017. Blood Flow in the Microcirculation. Annual Review of Fluid Mechanics 49:443–461.

[10] Yang, S., A. Ündar, and J. D. Zahn, 2006. A microfluidic device for continuous, real time blood plasma separation. Lab on a Chip 6:871–880.